Diverse mixing state and ice nucleation properties of aerosol particles over the Western Pacific and the Southern Ocean

Jiao Xue[1], Tian Zhang[1], Keyhong Park[2], Jinpei Yan[3], Young Jun Yoon[2], Jiyeon Park[2,*], Bingbing Wang[1,4,*]

[1] State Key Laboratory of Marine Environmental Science, College of Ocean and Earth Sciences, Xiamen University, Xiamen, 361102 China

[2] Korea Polar Research Institute, Incheon, 21990 South Korea

[3] Third Institute of Oceanography, Ministry of Natural Resources, Xiamen 361005, China

[4] Center for Marine Meteorology and Climate Change, Xiamen University, Xiamen, 361102 China

Correspondence: Bingbing Wang (Bingbing.Wang@xmu.edu.cn) and Jiyeon Park (jypark@kopri.re.kr).

Abstract

Atmospheric particles can impact cloud formation and play a critical role in regulating cloud properties. However, particle characteristics at the single particle level and their ability to act as ice nucleating particles (INPs) over the marine atmosphere are poorly understood. In this study, we present micro-spectroscopic characterizations and ice nucleation properties of particles collected during a cruise from South Korea to Antarctica in 2019. Most of the samples were dominated by fresh sea salt, aged sea salt, and sea salt mixed with sulfate particles, with total number percentages ranging from 48% to 99% over the Western Pacific and the Southern Ocean. The mixing state index of the particle population ranged from 50% to 95% over the northern and southern hemispheres. Multiphase processes on sea salt particles resulted in chlorine deficiency. This selective aging process made the marine particle population more externally mixed. Ice nucleation onset conditions were measured and the investigated particles showed diverse ice nucleation abilities. The fresh sea salt particles with organic coatings exhibited the highest ice nucleation ability at a relative humidity with respect to ice as low as 121%. The sea salt mixed sulfate particle was enriched in INPs by a factor of 1.9. Aging processes affected both particles' mixing state and their ice nucleation abilities. Our analysis shows that assuming an internally mixed particle population in the marine atmosphere can lead to errors of several orders of magnitude in predicting ice nucleation rates.

Keywords: Ice nucleation, ice nucleating particles, single particle analysis, marine aerosols, elemental composition, mixing state

1. Introduction

As 70.8% of the Earth's surface is covered by oceans, marine aerosol particles are one of the most important types of natural aerosols in the global inventory (Myriokefalitakis et al., 2010; De Leeuw et al., 2011). Aerosols in marine environments can affect the ocean biogeochemical cycles and indirectly or directly affect Earth system's radiation budget (Song et al., 2022). The sixth Intergovernmental Panel on Climate Change (IPCC) assessment report highlights a significant uncertainty in predicting the net effective radiative forcing of aerosols, with aerosol-cloud interactions contribute the most (IPCC, 2021). The impacts of atmospheric particles on cloud microphysical processes are still poorly understood (IPCC, 2013). The physicochemical properties of particles determine their abilities to serve as cloud condensation nuclei (CCN) and INPs, thereby affecting cloud microphysical processes. Particles serving as INPs can potentially trigger ice nucleation via four pathways: (1) deposition ice nucleation (DIN), which forms ice by the direct deposition of water vapor onto particle surface; (2) immersion freezing (IMF), which droplet freezing is triggered by immersed particles; (3) contact freezing, when droplets freeze by the contact with particles; (4) condensation freezing, when droplets freeze as water vapor condenses on droplets or particles. The majority of recent studies have focused on the IMF and DIN under mixed-phase and ice cloud conditions (Hoose and Möhler, 2012; Murray et al., 2012; Kanji et al., 2017; Knopf et al., 2018).

Diverse sources and atmospheric processes bring great challenges to the study of the physicochemical properties of marine particles. One of the major particle types in the marine atmosphere is sea spray aerosol (SSA) generated from wave breaking and bubble bursting over the ocean surface. Their compositions are mainly affected by seawater, sea ice, and biological activities and have minimum influence from anthropogenic activities (Kunwar et al., 2023). Other sources may also contribute to marine aerosols, such as ship emission (Ault et al., 2009, 2010) and long-range transport of aerosols from industrial emission, biomass burning, dust storms, and fossil fuel

combustion (Han et al., 2006; Fu et al., 2013; Geng et al., 2019). In addition, atmospheric oxidation of volatile organic compounds from the ocean or anthropogenic activities results in gas-particle conversion, multiphase reactions, and the formation of secondary materials on particles (Cochran et al., 2017). For example, dimethyl sulfide (DMS) from marine sources can be oxidized to form methanesulfonic acid (MSA) and sulfuric acid (H_2SO_4) in the atmosphere (Barnes et al., 2006; Chen et al., 2018; Berndt et al., 2023). Moreover, multiphase reactions can occur on the surface or within particles causing changes in the physicochemical properties of particles (Cochran et al., 2017). The oxidation products of DMS (H_2SO_4 and MSA) can react with sea salt particles resulting in chloride depletion from acid displacements (Liu et al., 2011).

Due to the diverse sources and dynamic evolution in the atmosphere, individual particles become mixtures of various compositions and have complex morphologies. Chemical mixing state is a term used to describe how various chemical species are mixed within individual particles in an aerosol population (Riemer et al., 2019). Riemer and West (2013) proposed a framework to quantify the chemical mixing state, which is described later in Section 2.3. Quantifying the chemical mixing state helps us to discuss how the population with different internal or external mixing affects its optical properties, cloud formation properties, and climatic impacts (Riemer et al., 2019). It is necessary to study the physical and chemical characteristics of individual particles as well as how they are mixed in the population to quantify the fundamental details of cloud microphysical processes (Cziczo et al., 2017; Kanji et al., 2017; Knopf et al., 2018; Riemer et al., 2019; Burrows et al., 2022). Using single-particle techniques, previous studies have focused on mixing states including but not limited to marine particles (Ault et al., 2010; Park et al., 2014; Tomlin et al., 2021), biomass burning aerosol (BBA) (Tomlin et al., 2022; Healy et al., 2013), and dust particles (Fraund et al., 2017; Adachi et al., 2020). Previous studies have quantified the chemical mixing state of an aerosol population using the mixing state index (χ), which is based on the mass percentages of various chemical species in single particles within a population (Riemer et al., 2019). However, there have been limited studies focusing on quantifying

101 χ from single particle component information of marine particles.

102

103 Laboratory and field studies have shown that various particle types have potential
104 impacts on atmospheric ice crystal formation. Natural INPs include mineral dust, soil
105 particles, volcanic ash, SSA, BBA, and bioaerosols. Anthropogenic INPs include
106 agricultural particles, metals and metal oxides from industrial processes, and fossil fuel
107 combustion particles (Hoose and Möhler, 2012; Murray et al., 2012; Kanji et al., 2017).
108 For marine related particles, Schill and Tolbert (2014) found that SSA are efficient INPs
109 below 225 K. Wagner et al. (2018) showed that SSA and desert dust particles share the
110 same order of magnitude of ice nucleation active surface site density (n_s) for deposition
111 nucleation. Previous studies have also shown that n_s for SSA is 2-3 orders of magnitude
112 lower than that for dust particles in immersion freezing (DeMott et al., 2016;
113 McCluskey et al., 2018a; Cornwell et al., 2019). Knopf et al. (2011) confirmed that
114 intact cells or fragments of marine diatoms can act as INPs. Wilson et al. (2015)
115 demonstrated that the sea surface microlayer is enriched with ice nucleating materials.
116 McCluskey et al. (2018b) identified two types of INPs from mesocosm experiments,
117 which were dissolved organic carbon coated particles and particulate organic carbon
118 particles like intact cells or cell fragments from microorganisms. Alpert et al. (2022)
119 confirmed that INPs in the SSA were the sea salt with organic matter, which were
120 exudates released from planktonic microorganisms. Inoue et al. (2021) found high INP
121 concentrations under high wave conditions which were related to the release of organic
122 carbon from the ocean. Welti et al. (2020) collected the INP concentration data over the
123 Arctic, Atlantic, Pacific, and Southern oceans. They found that ship-based INP
124 measurements over the oceans were 1 to 2 orders of magnitude lower than continental
125 observations. INP concentrations were lowest in the polar regions and highest in the
126 temperate climate ocean (Welti et al., 2020). Most of the field investigations over
127 oceans focus on the INP concentration measurements for IMF and at mixed-phase cloud
128 conditions with relatively warmer temperatures (Hoose and Möhler, 2012; Murray et
129 al., 2012; Kanji et al., 2017; Knopf et al., 2018). Recent field studies have used
130 advanced micro-spectroscopes and mass spectrometry to image and characterize the

INPs and ice crystal residuals to understand their nature (e.g., Cziczo et al., 2017; Knopf et al., 2018). INPs and ice residuals are often mixtures of chemical species. Ice nucleation is inherently related to the mixing state of particles because it depends on the particle surface properties. Quantifying the ice nucleation rate also depends on the details of composition, surface area, and the mixing state of the particle population. The importance of mixing state for INPs is well recognized, but there are limited studies focusing on its quantification which is poorly understood (Kanji et al., 2017; Knopf et al., 2018; Riemer et al., 2019).

In this study, we quantified ice formation potential and elemental composition of particles over coastal and open oceans using microscope-based ice nucleation instrumentation and computer-controlled scanning electron microscopy with energy dispersive X-ray spectroscopy (CCSEM/EDX), respectively. The mixing state of particle population based on the elemental composition was derived for 29 marine ambient particle populations extending from the northern to the southern hemisphere. Ice nucleation onset conditions were measured and the INPs were identified for representative samples. Individual INPs were characterized and compared with the particle population to relate ice nucleation ability to the mixing state. Potential errors in predicting ice nucleation rate were briefly discussed if models assume an internally mixed population. We performed ice nucleation kinetic analysis based on the experimental data and provided parameterizations for cloud modeling.

2. Experimental methods

2.1 Particle sampling

Aerosol particles were collected by a four-stage cascade impactor (SKC, Inc.) at a sample flow of 9 L min^{-1} on board the Korean ice breaker R/V *Araon* from October 31st to December 12nd in 2019. Particles were collected on the third and fourth stages of the impactor with 50% collection efficiency at aerodynamic sizes of 0.5 μm and 0.25 μm, respectively. The inlet was located on the third deck of the ship at about 13 m above sea

surface level (Park et al., 2020). As shown in Fig. 1, the cruise crossed about 110 degrees of latitude from the Western Pacific near South Korea (34.93°N) to the Ross Sea in the Southern Ocean (75.12°S). Samples were collected on transmission electron microscopy (TEM) copper grids (Carbon Type-B, Ted Pella, Inc.) for single particle analysis by CCSEM/EDX and silicon wafer chips (Silson, Ltd.) with the hydrophobic coating (Si_3N_4) for ice nucleation experiments following our previous studies (Wang et al., 2012a, 2016a; Knopf et al., 2014). Particles were collected simultaneously on these two substrates which were placed side by side in the same impactor. Particle samples were stored at room temperature in an airtight container with desiccant until analysis. This study focuses on deposition ice nucleation at low temperatures and INP identification. Particles with a smaller size range may have a longer lifetime and can potentially be transported to higher altitudes in the atmosphere. Therefore, we limited our analysis to the samples collected on the fourth stage. Meteorological conditions and black carbon concentrations were measured by the onboard weather station and an aethalometer (AE22, Magee Scientific Co., USA), respectively. When the relative wind direction against the ship heading is between 110° and 260° and the relative wind speed is below 2 m s^{-1}, samples may have been influenced by the ship exhaust (Park et al., 2020). Potentially contaminated samples were excluded from the analysis, resulting in a total of 29 selected samples. The sampling location and 72 h backward air mass trajectories are shown in Fig. 1. Backward air mass trajectories were computed using the Hybrid Single-Particle Lagrangian Integrated Trajectory (HYSPLIT) model (Stein et al., 2015; Rolph et al., 2017). Detailed sampling information is listed in Table S1 and includes the collecting time, location, and the corresponding meteorological data. Black carbon concentration, air temperature, relative humidity, pressure, relative wind speed, and wind direction are also shown in Fig. S1.

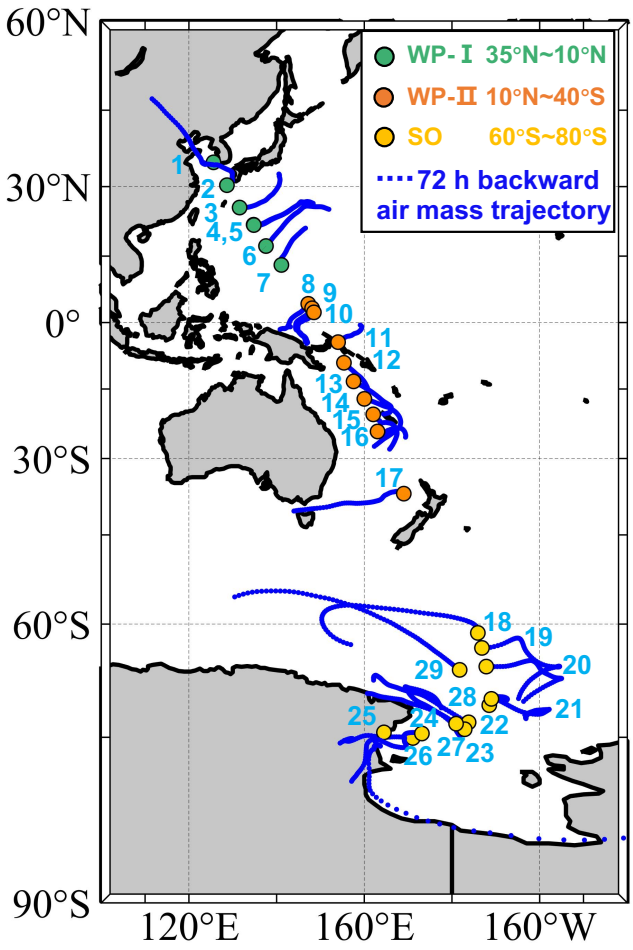

185

186 **Figure 1.** Sampling locations with HYSPLIT 72 h backward air mass trajectories. Solid circles
187 indicate the sample locations. Samples were labeled by numbers. Green, orange, and yellow circles
188 represent the samples in 35°N – 10°N of Western Pacific (WP-I), 10°N – 40°S of Western Pacific
189 (WP-II), and 60°S – 80°S of Southern Ocean (SO) regions, respectively. Blue lines show the
190 backward trajectories starting from 100 m above sea level.

191

192 **2.2 Chemical imaging and characterization of particles and INPs**

193 Chemical imaging and single particle analysis were used to obtain information on the
194 morphology, size, and elemental composition of the particle population and INPs. The
195 methods have been described in detail in previous work (Laskin et al., 2002, 2006, 2012;
196 Wang et al., 2012a; Knopf et al., 2014; O'Brien et al., 2015) and are briefly introduced
197 here. Samples collected on the TEM grids were analyzed using a scanning electron
198 microscopy (Quanta 650, FEI Inc.) equipped with an energy dispersive X-ray

spectroscopy (Genesis, EDAX Inc.) in the computer-controlled mode (CCSEM/EDX). CCSEM/EDX operating at 20 kV first detected the particles and determined their size. The particle size reported here is the equivalent circle diameter (ECD) based on the two-dimensional projected area of the particle as determined by CCSEM/EDX analysis. Particles with a size (ECD) between 0.2 μm and 3 μm were included for analysis in this study. The elemental composition of each particle was then quantified by determining the relative atomic percentages of the selected elements, including C, N, O, Na, Mg, Al, Si, P, S, Cl, K, Ca, Mn, and Fe. We obtained the elemental composition for a significant number of particles, about 630 – 1480 particles for each sample depending on the particle loading on the substrates (Table S1). We manually performed SEM/EDX analysis to characterize the individual identified INPs on the silicon wafer chips after ice nucleation experiments, as described later. In addition, about 10 particles that did not nucleate ice (non-INPs) were randomly selected around each INP for SEM/EDX analysis. X-ray spectra for the INPs and non-INPs were collected at 10 kV. The relative atomic percentages of elements including C, O, Na, Mg, Al, P, S, Cl, K, and Ca were quantified. N and Si were not included in the quantification due to their presence in the background substrate.

The relative atomic percentage data were analyzed using a rule-based classification method to assess the contributions of different particle types for each sample (Laskin et al., 2012; Wang et al., 2012a; China et al., 2018; Lata et al., 2021). As shown in Fig. 2, the classification scheme grouped particles into seven classes: *i*) "CNO" particles, which mainly contain C, N, and O elements with traces of other elements. These are carbonaceous particles such as black carbon, secondary or primary organic particles. *ii*) "CNOS" particles, which mainly contain C, N, O, and S elements with traces of other elements and are sulfates and other sulfur containing particles including their internal mixtures with organics. *iii*) "FreshSS" particles, these are fresh sea salt particles containing Na above a threshold level of 2% (atomic percentage) and the Cl/Na ratio is > 0.8. At the same time, the total atomic percentage of Na, Mg, and Ca, which are the dominant cations in sea salt particles, is higher than that of other metals. CCSEM/EDX

analysis of fresh sea salt particles generated by nebulizing sea water shows that the Cl/Na ratio is slightly higher than 0.8 for particles at about 0.2 μm (Fig. S2). The samples we investigated contain a large number of small sea salt particles. Thus, we use a Cl/Na ratio of 0.8 as the threshold value to distinguish between the fresh and aged sea salt particles. *iv*) "AgedSS" particles, these are aged sea salt particles with Cl depletion and the Cl/Na ratio < 0.8. *v*) "SS/Sulf" particles, these are aged sea salt particles mixed with sulfur-containing compounds (e.g., sulfate) containing mainly Na and S without Cl. *vi*) "Dust" particles, these particles have the total atomic percentage of Al and Si above 4% and higher than the total atomic percentage of Na and Mg. They are likely from dust storms and road or soil emissions. *vii*) "Mixture" particles are all remaining particles that did not fit into the previous categories. The classification scheme for INPs and non-INPs on silicon wafer chips was modified to account for the Si and N background in the substrate. It is important to note that particles on either TEM grids or Si chips were collected at the same time using the same impactor, and therefore the contributions of the respective particle classes for the two are the same. Thus, we modified the classification scheme with this assumption.

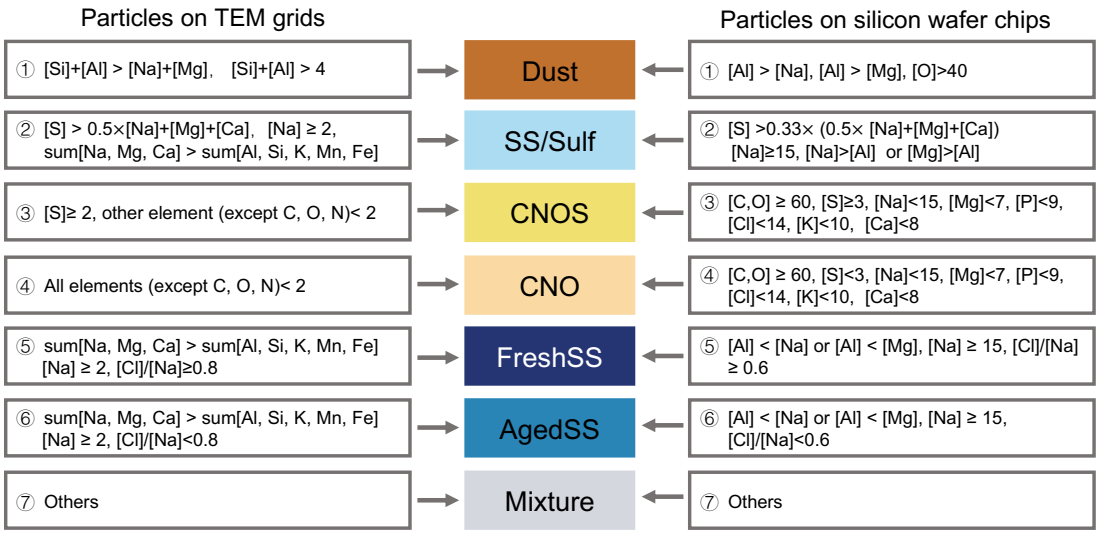

Figure 2. Rule-based particle classification schemes for particles on TEM grids (left) and silicon wafer chips (right). Numbers in the schemes are the relative atomic percentages of corresponding elements or their ratios.

250

251 **2.3 Chemical mixing state**

252 Chemical mixing state was derived using a previous methodology based on mass and
253 entropy metrics (O'Brien et al., 2015; Riemer and West, 2013) and is described briefly
254 here. Particle mass was estimated from the density and volume of each particle.
255 Particles were assumed to be hemispherical and the volume of each particle was
256 calculated from the ECD obtained by CCSEM. Particle density was assigned according
257 to its classification, with FreshSS, AgedSS, SS/Sulf, CNO, CNOS, Dust, and Mixture
258 particles having a density of 2.0 g/cm^3, 2.0 g/cm^3, 1.7 g/cm^3, 1.3 g/cm^3, 1.3 g/cm^3, 2.7
259 g/cm^3, and 2.0 g/cm^3, respectively (O'Brien et al., 2015; Tang et al., 2014). To calculate
260 the mass of each element in a particle, the atomic percentage of each element obtained
261 by EDX was converted to a weight percentage, and then multiplied by the mass of the
262 particle. For the particle i, the mass of element a is equal to:

263 $$\mu_i^a = \mu_i \left(\frac{elemental\%^{a} \times molar\ mass^{a}}{\sum_{a=1}^{A} elemental\%^{a} \times molar\ mass^{a}} \right) \quad (1)$$

264 Where a = 1, …, A (number of elements), i = 1, …, N (number of particles), and μ_i is
265 the total mass of the i^{th} particle. a represents elements of Na, Mg, Al, Si, P, S, Cl, K, Ca,
266 Mn, and Fe, and for this list, A = 11. Note that C, N, and O are not included as these
267 three elements are semi-quantitative when EDX analysis is used (Laskin et al., 2006).

268

269 First, the total mass of element a in the particle population (μ^a), and the total mass of
270 the bulk particle population (μ) were calculated using the following equations,

271 $$\mu^a = \sum_{i=1}^{N} \mu_i^a \ , \quad (2)$$

272 and

273 $$\mu = \sum_{i=1}^{N} \mu_i \ . \quad (3)$$

274 Then, the mass fraction of element a in the i^{th} particle (p_i^a), the mass fraction of
275 individual particles (p^i) in the particle population, and the mass fraction of element a in
276 the bulk particle population (p^a) are

$$p_i^a = \frac{\mu_i^a}{\mu_i}, \quad (4)$$

$$p_i = \frac{\mu_i}{\mu}, \quad (5)$$

and

$$p^a = \frac{\mu^a}{\mu}. \quad (6)$$

Next, the following Shannon entropies (MacKay, 2003) were calculated, where the mixing entropy of the i^{th} particle (H_i) is

$$H_i = \sum_{a=1}^{A} -p_i^a \, lnp_i^a, \quad (7)$$

the average particle mixing entropy (H_a) is

$$H_a = \sum_{i=1}^{N} p_i H_i, \quad (8)$$

and the mass entropy of bulk particle population (H_γ) is

$$H_\gamma = \sum_{a=1}^{A} -p^a lnp^a. \quad (9)$$

H_i and H_γ are used to describe the mass distribution of species (elements) with the i^{th} particle or particle population, respectively. A higher entropy indicates a more uniform distribution of elements in the individual particle or particle population whereas a lower entropy towards a non-uniform mass distribution.

Individual particle diversity (D_i) is calculated by taking the exponent of H_i. D_i means the effective number of elements in individual particles, or in other words, indicates the distribution of elements in single particles. D_i ranges from the minimum value of 1 when the particle contains a single element to the maximum value of A when the particle is composed of all A elements with equal mass. Particle elemental diversity (D_α) and bulk population elemental diversity (D_γ) are calculated by taking the exponent of H_a and H_γ, respectively. D_α indicates the average effective number of elements in particles. D_γ indicates the effective number of elements in the whole particle sample.

$$D_i = e^{H_i} = \prod_{a=1}^{A} (p_i^a)^{-p_i^a} \quad (10)$$

$$D_\alpha = e^{H_\alpha} = \prod_{i=1}^{N} (D_i)^{p_i} \quad (11)$$

$$D_\gamma = e^{H_\gamma} = \prod_{a=1}^{A} (p^a)^{-p^a} \quad (12)$$

Mixing state index (χ) indicates the homogeneity or heterogeneity of the population and is defined as

$$\chi = \frac{D_\alpha - 1}{D_\gamma - 1} . \quad (13)$$

χ ranges from 0% for an externally mixed particle sample with a heterogeneous population composing single-component particles (D_α = 1) to 100% for an internally well mixed particle sample with a homogeneous population where all particles have identical compositions.

2.4 Ice nucleation experiment and INP identification

Ice nucleation and water uptake by particles were examined following our previous studies (Knopf et al., 2011, 2014, 2022; Wang and Knopf, 2011; Wang et al., 2012b; Charnawskas et al., 2017; China et al., 2017; Alpert et al., 2022) and the methods are briefly introduced here. Onset conditions of the particle temperature (T_p) and relative humidity with respect to ice (RH_{ice}), when ice nucleation and water uptake occurred, were determined using a custom-built cryo-cooling system. The system consists of a water vapor control component, an ice nucleation cell (INC), and an optical microscope (OM). Prior to ice nucleation experiments, a particle sample collected on a silicon wafer was placed in the INC. Then, a humidified N_2 gas with targeted water vapor partial pressure was continuously introduced into INC at a flow rate of one standard liter per minute. The water partial pressure in the INC was determined by the dew point temperature (T_d) of the gas which was measured using a chilled mirror hygrometer (GE Sensing, Optica). After T_d was stable, T_p was set to about T_d + 3 K and RH_{ice} < 100%. An ice nucleation experiment was started and T_p was cooled at a rate of 0.2 K min^{-1}.

Images of particle sample were recorded by OM every 0.02 K. T_d and T_p were recorded every second throughout the experiment. Once ice formation was observed, the sample was gradually warmed to 298 K to sublime and remove any ice that may be retained in the pores or cavities of particles. Images of ice crystals were acquired during sublimation at high magnification and the visible particle that served as the INP was identified after complete crystal sublimation. The experiment was repeated 3 – 7 times at similar T_d for reproducibility. Water uptake and ice formation by particles were determined through visual observation and the changes in particle phase or size from analyzing the recorded images using ImageJ software. through visual observation. DIN and IMF were discriminated based on whether particles took up water before ice formation. The freezing mechanism within the small droplets after the water uptake could not be visualized due to the limited spatial resolution and imaging speed of the OM used in this study. Thus, we assume that immersion freezing has occurred if the RH_{ice} onset of freezing is lower than the homogeneous freezing limits. Only the temperature and RH_{ice} conditions when the first ice crystal formed were reported. RH_{ice} was derived from the measured T_d and T_p (Wang and Knopf, 2011). Particle surface area available for ice nucleation for each sample was estimated from the particle number and size derived from OM images, assuming that the particles were hemispheres. The conservative uncertainty of a factor of 2 for particle surface area was estimated using the standard deviation of the means with assumption of particles being flat or spherical. This assumption likely underestimates the actual surface area since most of the particles deposited on the substrate exhibited non-spherical geometry and may have had rough surfaces including cracks or cavities. The particle surface areas were later used for ice nucleation kinetic analysis. INPs were identified using the recorded optical images during ice nucleation, ice growth, and ice sublimation. Using these optical images, INPs were relocated in the SEM using digital pattern recognition and triangulation and then were imaged and analyzed by SEM/EDX (Knopf et al., 2014).

The temperature and water vapor distribution within the INC were calibrated and validated following our previous work (Wang and Knopf, 2011; Wang et al., 2016b).

Homogeneous water vapor distribution in the INC was confirmed by uniform condensation and evaporation of micro-meter size water droplets across the 0.5 mm^2 sample area. T_p was calibrated by the melting points of ice, dodecane, decane, octane, and heptane. The calibration confirmed that the response of T_p is linear in the range of 180 – 273 K with an uncertainty less than 0.3 K. Conservative uncertainty in RH_{ice} for this experimental system comes from the uncertainty in T_d and T_p ($\Delta T_d < \pm 0.15$ K and $\Delta T_p < \pm 0.3$ K), resulting in $\Delta RH_{ice} < \pm 11\%$ at 200 K and $\Delta RH_{ice} < \pm 3\%$ at 260 K.

3. Results and discussion

3.1 Particle characterization

Figure 3 shows the typical SEM images and the corresponding EDX spectra of the identified particle classes. FreshSS and AgedSS particles were dominated by Na with different contents of Cl. The FreshSS particle exhibited a cubic NaCl crystal morphology (black solid square) with irregular materials (bright coating) under the transmission detector of SEM at darkfield mode. The coating likely comprised other materials in seawater including $MgSO_4$ and $CaSO_4$ (Xiao et al., 2008). The AgedSS particle showed a non-cubic shape NaCl crystal shape as its core surrounded by substances containing Na with depletion of Cl. The depletion of Cl indicates that the particle had been aged, possibly due to the formation of gaseous HCl by chemical reactions with nitric acid, sulfuric acid, and organic acids in the atmosphere (Laskin et al., 2012; Wang et al., 2015; Angle et al., 2021; Su et al., 2022). The SS/Sulf particle showed in Fig. 3 had a core-shell structure and was mainly composed of Na and S without Cl. This suggests that it was a completely aged sea salt particle coated with sulfur-containing components, such as sulfate. The CNOS and CNO particles showed a round-shaped morphology. The Dust-like particle exhibited clear Al and Si peaks with minor Ca. Figure 4 shows the particle classification results of over 30,000 particles in 29 samples investigated by CCSEM/EDX. The size-resolved chemical distributions for all samples are shown in Fig. S3, with FreshSS and AgedSS particles dominating all size bins. The majority of SS/Sulf particles were larger than 0.5 μm, while the CNOS

and CNO particles were mainly in the sub-micrometer size range. As shown in Fig. 1 and Fig. 4, the samples (S1 – S29) were separated into the following three regions according to the latitudes of the sampling locations, 35°N – 10°N of the Western Pacific (WP-I), 10°N – 40°S of the Western Pacific (WP-II), and 60°S – 80°S of the Southern Ocean (SO).

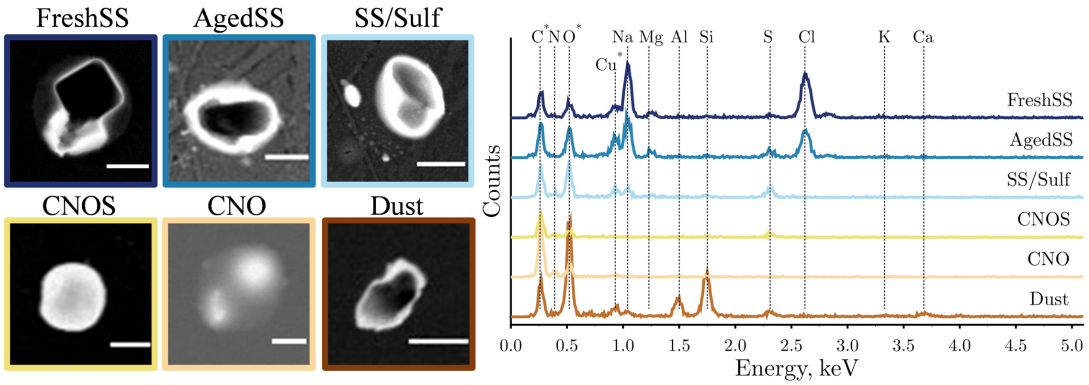

Figure 3. Representative SEM images and the corresponding EDX spectra for particles from each class. The peaks in spectra for the C, O, and Cu elements (asterisked) may include some signal from substrate background of TEM grids. SEM images were captured at 20 kV using scanning transmission electron microscopy detector. The scale bar for all images is 1 μm.

Figure 4 shows that in the WP-I region (35°N – 10°N, S1 – S7), the proportion of FreshSS and AgedSS particles increased from 10% to 91% as the ship moved away from the land, indicating an increased contribution of SSA. The contribution of the Dust particle class decreased from 59% to 8% for S1 to S3. The Navy Aerosol Analysis and Prediction System reanalysis (NAAPS-RA) product indicated a dust storm during the S1 and S2 sampling periods (Fig. S4). The 72 h backward air mass trajectories also showed that the air mass passed through areas affected by the dust storm.

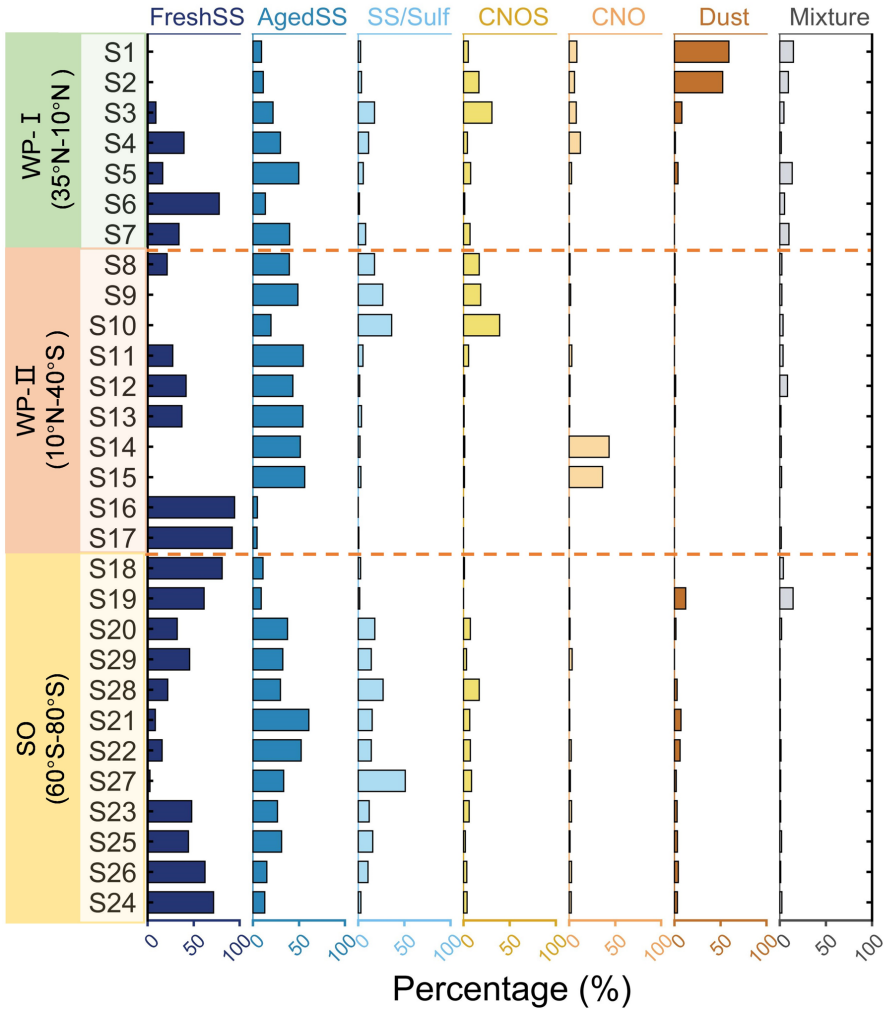

Figure 4. Relative percentages of the seven particle classes (FreshSS, AgedSS, SS/Sulf, CNOS, CNO, Dust, and Mixture) for each sample sorted by the latitudes of sampling locations and separated into three regions (see Fig. 1).

In the WP-II region (10°N – 40°S, S8 – S17), the backward trajectories (Fig. 1) display that the air mass of most samples resided over the ocean. However, the samples demonstrated large variations in the particle composition. S8 – S10 were dominated by AgedSS, SS/Sulf, and CNOS particles. The percentage of SS/Sulf and CNOS particles increased from 18% to 36% and from 17% to 39%, respectively, from S8 to S10. The contributions of these two sulfur-containing particle classes increased simultaneously, implying the same sulfur source. This is consistent with the results showing high sulfate aerosol optical depth (AOD) from the NAAPS-RA products at the same period (Fig. S4D – F). The average BC concentration was 107.4 ± 70.6 ng/m^3 for S8 (Table S1). It

likely originated from combustion emissions transported from land. As shown in Fig. S4C, this is further supported by the air mass for S8 passed through the region where fire spots were detected in NASA Fire Information for Resource Management System (FIRMS). S14 and S15 were dominated only by the AgedSS and CNO particles, with the latter accounting for 43% and 36%, respectively. These higher fractions of CNO particles compared to other samples (Fig. 4) are likely related to BBA. As shown in Fig. S1, the average BC concentrations of S14 and S15 were as high as 674 and 356 ng m^{-3}, respectively. Backward trajectories showed that the air mass passed through the high smoke AOD regions (Fig. S4G – H). These two samples were collected on November 13th and 14th of 2019, when large wildfires occurred in Australia during the austral summer of 2019 – 2020 (Hirsch and Koren, 2021). Dense fire spots along the east coast of Australia at the time of sampling are shown in Fig. S4I. Chemical imaging of elements (Fig. S5) showed that typical CNO particles from these two samples had thick organic coatings with high carbon signal inclusions and likely are aged BC. This type of aged BBA or smoke particles with organic coatings has been observed in the stratosphere (Ditas et al., 2018). Similar complex organic compounds have also been observed in the tropospheric smoke aerosol (Palm et al., 2020). Other samples in the WP-II region (S11, S12, S13, S16, and S17) were dominated by the FreshSS and AgedSS particles.

In the SO region (60°S – 80°S, sample S18 – S24), the number percentages of FreshSS particles decreased first and then increased as moving toward higher latitude, whereas the AgedSS, SS/Sulf, and CNOS particles had opposite trends. These three particle types contributed to 11% to 93% of the total particles in the sample. As shown in Fig. S6, the contributions of AgedSS, SS/Sulf, and CNOS particles from the middle of the Ross Sea (S28, S21, S22, S27, S23) were significantly higher than those from the north (S18, S19, S20, S29) and southwest (S25, S26, S24) of the Ross Sea. The increased contribution of these three sulfur-containing particle classes may be related to the biogenic sulfur emission from polynyas (areas of open water surrounded by sea ice) in the central Ross Sea (Fig. S7) (Brean et al., 2021; Baccarini et al., 2021; McCoy et al.,

2021; Jang et al., 2019; Zhang et al., 2015). The formation of polynyas during the austral summer allowed phytoplankton to grow and produce DMS. DMS is transferred into the atmosphere and oxidized. The products increase the sulfur content in aerosol particles. Previous works indicated that the MSA concentration over the Southern Ocean was about two times higher than that of the Western Pacific (Kunwar et al., 2023). High MSA levels were observed in the Ross Sea and were associated with the dynamic sea ice edge at ~64°S in early December (Yan et al., 2020). This was caused by the increase in phytoplankton from the release of algae from the melting sea ice. This also suggests the potential impacts by the biogenic emission of DMS on these samples.

Except for the two samples impacted by the dust storm, most of the samples collected during this cruise were predominantly sea salt containing particles including the FreshSS, AgedSS, and SS/Sulf classes, with total number percentages ranging from 48% to 99%. The varying proportions of these three particle classes indicated the contribution of marine emission, but with different degrees of aging which will be discussed in the next section. Figure S8A and Fig. S9A show the classification results for super-micron particles (diameter > 1 μm) and submicron particles (diameter between 0.2 and 1 μm), respectively. The sea salt containing particles including FreshSS, AgedSS, and SS/Sulf classes had higher percentages in the super-micron size range. The majority of CNOS particles were in the submicron size range. CNOS represents sulfur containing particles (e.g., sulfate) including their mixtures with organics. CNOS particles were predominantly in the submicron range, likely due to new particle formation of MSA and H_2SO_4 and their condensation onto pre-existing particles (Hopkins et al., 2008; Yan et al., 2020; Beck et al., 2021). Heterogeneous aqueous chemical reactions may also contribute to CNOS particles, including cloud processing (e.g., Ervens et al., 2018).

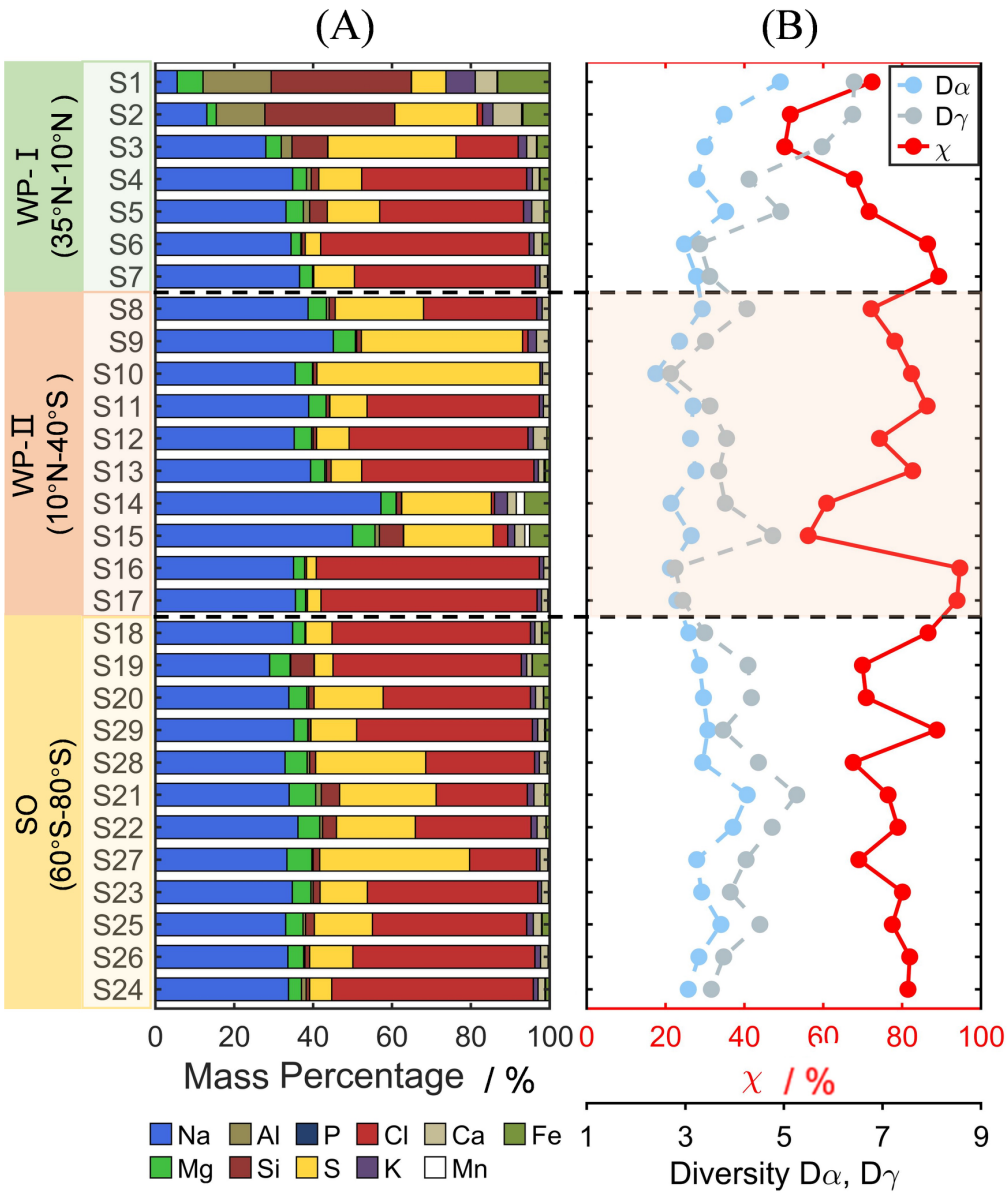

Figure 5. Relative mass percentages of elements (A), and mixing state (B) of all samples. Color codes for the elements are shown at bottom. Light blue, gray, and red circles represent the particle elemental diversity (D_α), population elemental diversity (D_γ), and mixing state index (χ), respectively.

3.2 Mixing state of particle population

Mixing state described here is based on the elemental composition and is referred to as the chemical mixing state. Figure 5A shows the elemental mass percentages of the particle population for each sample. Most of the samples were dominated by Na, Cl, and S, except the samples affected by dust storm (S1, S2). The proportion of Na in each

sample was relatively stable at about 38%. The rest was contributed mostly by Cl and S. The aging of sea salt particles can be evaluated by the elemental ratio of Cl to Na (Cl/Na). As shown in Fig. 5A and Fig. S10, the Cl/Na ratio ranges from 0 to close to 1 indicating complete Cl depletion and no aging on sea salt particles, respectively. The samples with more S have less Cl. This is consistent with the increase in the proportion of sea salt with different degrees of aging (AgedSS and SS/Sulf). The relationship between S and Cl indicates that the chlorine loss in particles over ocean is attributed to the acid displacement by H_2SO_4 and MSA. The samples affected by the dust storm were dominated by the elements of Si, Al, and Fe, all of which were common in mineral dust with traces of Ca and K. As the elements of C, N, and O were not considered in the mass percentage calculation, the CNO particles prominent in S14 and S15 are not reflected in the mass percentages (Fig. 5A). The elements of K, Si, and Fe presented in the same samples are related to biomass burning (Chen et al., 2017). It is consistent with the air mass from which they were sampled being impacted by biomass burning plumes.

The mixing state parameters, namely D_α, D_γ, and χ for each sample, are presented in Fig. 5B. The range of D_α and D_γ was from 2.4 to 4.9 and 2.7 to 6.4, respectively. χ ranged from 50% to 95%. In the WP-I region, the Dust-dominated S1 had the highest D_α of 4.9 and D_γ of 6.4. As the contribution of the Dust particles decreased from 59% to 1% for S1 to S4, D_α and D_γ decreased from 4.9 to 3.2 and 6.4 to 4.3, respectively. χ first decreased from 72% to 50% (S1 to S3) and then increased to 68% (S4) as the dominant particle type switched from Dust to sea salt containing particles. χ further increased to 86% (S6) when FreshSS particles dominated. In the WP-II region, D_α and D_γ decreased as CNOS and SS/Sulf particles increased and the mass percentage of S increased from S8 to S10, corresponding to a slight increase in χ from 72% to 82%. When comparing the wildfire-influenced samples (S14, S15) and the FreshSS dominated samples (S16, S17), the D_α values are very similar whereas D_γ values are quite different (3.8 and 4.8 vs. 2.8 and 2.9) resulting in contrasting χ values. The highest χ of about 95% for S16 and S17 indicated that these two samples dominated by Na and

517 Cl were largely internally mixed. This can be expected since they were dominated by
518 FreshSS particles from the single marine source. AgedSS particles from marine
519 emission with additional atmospheric processing and CNO particles from biomass
520 burning had similar contributions to S14 and S15. This was reflected in χ of about 58%
521 for S14 and S15. The main elements of Na and S in these two samples are more
522 externally mixed. In the SO region, D_α and D_γ were similar to each other resulting in
523 relatively stable χ values. The changes in D_α and D_γ are mainly due to the changes in
524 the contribution of sulfur containing particles. Figure S8 and Fig. S9 show the elemental
525 mass percentages, D_α, D_γ, and χ for super-micron and submicron particles, respectively.
526 For submicron particles of each sample, D_α and D_γ are 1.9 – 3.9 and 2.4 – 7.1,
527 respectively. χ ranges from about 38% to 95%. For super-micron particles of each
528 sample, D_α and D_γ are 2.5 – 5.1 and 2.7 – 6.6, respectively. χ ranges from about 54% –
529 96%. In general, D_α and χ for the submicron particles are lower than super-micron
530 particles in most samples, whereas D_γ is similar. This suggests that the main elements
531 of Na, S, and Cl and the minor elements of Mg, K, Fe, Ca, and Si in super-micron
532 particles tend to be more internally mixed than in submicron particles (Fig. S8B and
533 Fig. S9B).
534
535 The changes in the particle composition may affect the mixing state of the particle
536 population. To focus on the effect of particle aging on the mixing state of marine
537 aerosols, we excluded four samples from two events from the analysis, i.e., the Dust-
538 dominated samples from a dust storm (S1 and S2) and the BBA-dominated samples
539 from wildfire emissions (S14 and S15). Figure 6 shows the relationship between χ and
540 the percentages of FreshSS, AgedSS and SS/Sulf, and CNOS particles in different size
541 ranges. To minimize the potential influence of extreme data points, the linear regression
542 was performed using the binned data based on the number percentage of particle type.
543 We found a strong correlation between the percentages of FreshSS particles in the
544 samples and their χ (Fig. 6A, $R^2 = 0.66$, $p = 0.008$), especially for submicron particles
545 ($R^2 = 0.85$). χ increased as the contribution of FreshSS particles increased. There is a
546 negative correlation between χ and the total percentage of AgedSS and SS/Sulf particles

(Fig. 6B, $R^2 = 0.46$, $p < 0.05$). We also found a strong negative correlation between χ and the contribution of CNOS particles (Fig.6C, $R^2 = 0.86$, $p = 0.002$). The results of the above-mentioned relationship also hold for both submicron and super-micron size range particles. The positive correlation between the contribution of FreshSS particles and χ indicates that the particle population became more internally mixed as more fresh SSA were added to the air parcel. When the FreshSS particles became the dominant type, the particle population was close to the complete internal mixing ($\chi = 100\%$), such as S16 and S17 as discussed above. Here, we show that adding more particles of the dominant particle class (FreshSS) makes the population more internally mixed. Adding CNOS particles (a new particle class) decreases the χ and makes the population more externally mixed. These results verify the schematic description of the evolution of the mixing state described by Riemer et al. (2019). It states that adding new particle types makes the population more externally mixed and adding particles of a dominant particle type makes the population more internally mixed.

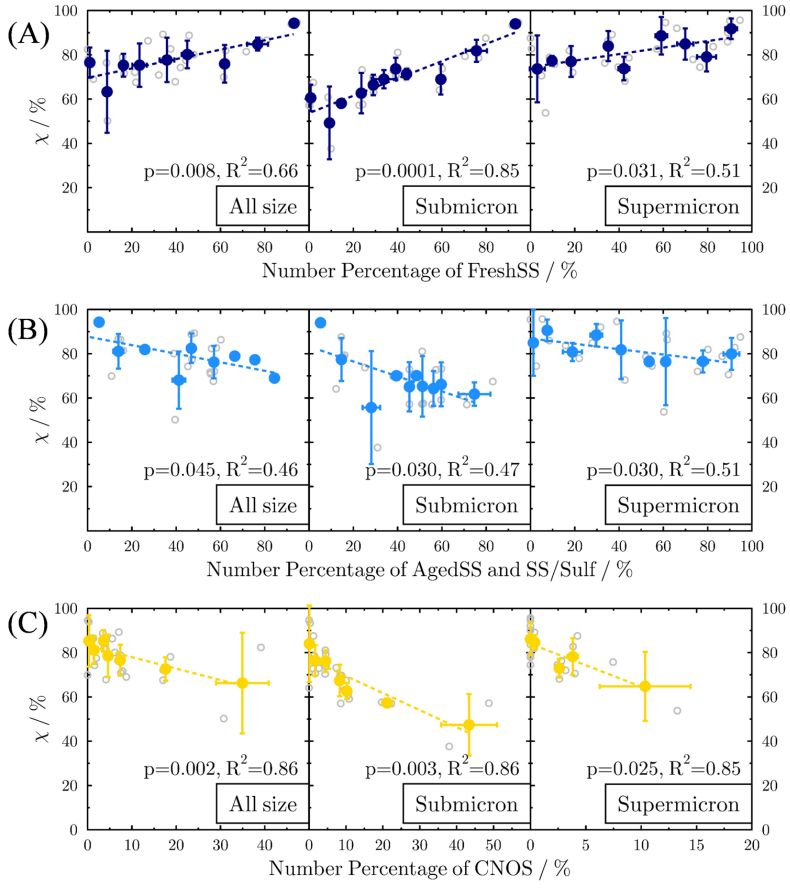

Figure 6. Variation of mixing state index (χ) with the number percentages of different particle classes: (A) FreshSS, (B) AgedSS and SS/Sulf, and (C) CNOS. Panels from left to right are for particles with different size ranges: all particle size (All size), 0.2 – 1 μm (Submicron), and larger than 1 μm in diameter (Super-micron). Original and binned data are shown in open circles and solid color circles, respectively. Linear regression (dash line) is based on the binned data.

Atmospheric aging processes can change the composition and mixing state of aerosol population. In marine environments, the degree of aging on sea salt particles can be reflected by the contribution of AgedSS and SS/Sulf particles in the population. The negative correlation between the number percentages of AgedSS and SS/Sulf particles and χ indicates that aging has resulted in a more externally mixed particle population. This seems to contradict the view that aging tends to drive a particle population towards a more internally mixed state (Riemer et al., 2019). If an aging process (e.g., condensation of secondary organics) occurs uniformly on each particle and further aging makes them more homogeneous, the population tends to be more internally mixed. On the other hand, if the aging process occurs only on a specific type of particle, such as acid displacement turning fresh sea salt into aged sea salt, this will increase particle diversity and the population may move to a more externally mixed state. This may be particularly true as fresh sea salt is continuously released even as aged sea salt particles form. The availability of acids and the size distribution of fresh and aged sea salt particles at different locations could result in particles with different chlorine deficiencies and greater diversity. In this case, aging will increase the inhomogeneity of particles and move the population toward a more externally mixed state.

3.3 Ice nucleation properties at cirrus conditions

We conducted ice nucleation experiments on six samples dominated by different particle classes. These samples are separated into four groups: *i*) Dust dominated sample (S1), where 59% of the particles are dust-like. *ii*) BBA influenced sample (S14). This sample was affected by biomass burning. CNO and AgedSS particles contributed 43% and 51%, respectively. *iii*) CNOS and SS/Sulf dominated sample (S10) with

593 percentages of 39% and 36%, respectively. *iv*) FreshSS and AgedSS dominated samples
594 (S4, S11, and S12). The number percentages of the FreshSS and AgedSS particles are
595 70%, 82%, and 85% for S4, S11, and S12, respectively. Table 1 shows the dominant
596 particle class, total particle surface area, number of particles available for ice nucleation
597 during the experiments, IN-activated fraction at ice nucleation onsets, average ECD of
598 INPs and non-INPs, and average ECD of INPs.
599
600 **Table 1.** Information of particle samples including the total particle surface area and number of
601 particles, IN-activated fraction at ice nucleation onset conditions, the average ECD of INPs and
602 non-INPs, and the average ECD of INPs.

Sample	Dominant particle type	Particle surface area ($\times 10^4$ μm^2)	Particle number ($\times 10^5$)	IN-activated fraction (‰)	ECD for INPs (μm)	ECD for all (μm)
WP-I-S1	Dust	4.35	0.85	0.12 – 0.24	2.53 ± 1.76	1.45 ± 0.98
WP-I-S4	FreshSS+AgedSS	0.54	1.29	0.08 – 0.15	0.99 ± 0.25	0.89 ± 0.25
WP-II-S10	CNOS+SS/Sulf	6.81	9.13	0.01 – 0.03	1.54 ± 0.56	1.21 ± 0.57
WP-II-S11	FreshSS+AgedSS	7.76	6.37	0.02 – 0.03	1.19 ± 0.63	1.03 ± 0.50
WP-II-S12	FreshSS+AgedSS	12.91	8.26	0.01 – 0.02	1.91 ± 1.20	1.22 ± 0.78
WP-II-S14	BBA	13.84	0.56	0.18	5.17 ± 3.12	2.50 ± 2.01

603
604 Figure 7 shows the onset conditions of T_p and RH_{ice} for water uptake and ice nucleation
605 on the representative samples. Below 235 K, only DIN was observed for the Dust and
606 BBA samples (Fig. 7A). Particles on the Dust sample nucleated ice heterogeneously at
607 RH_{ice} from 130% ± 9% to 153% ± 8% at T_p from 235 K to 209 K. These values are
608 below the homogeneous nucleation limits of aqueous droplets (Koop et al., 2000; Koop
609 and Zobrist, 2009). RH_{ice} onsets of the BBA sample ranged from 145% ± 5% to 169%
610 ± 1% at T_p from 229 K to 209 K. The RH_{ice} onsets were only about 3% below the
611 homogeneous nucleation limits between 220 K and 228 K, and thus the sample
612 dominated by BBA may not have been efficient heterogeneous ice nuclei. As T_p
613 decreased, the RH_{ice} onset of both the BBA and Dust samples gradually increased.
614 Particles on the Dust sample initiated DIN at RH_{ice} lower than the BBA sample by 7%
615 to18% at each T_p. For the CNOS and SS/Sulf dominated sample (Fig. 7A), particles
616 first took up water when RH_w reached about 83% and then froze via IMF or

homogeneous nucleation with RH_{ice} around the homogeneous line at the temperature close to 230 K. Particles formed ice via DIN below 225 K at RH_{ice} from 136% ± 4% to 159% ± 11%. Figure 7B shows that the ice nucleated on particles from the FreshSS and AgedSS dominated samples via DIN and IMF pathways. The transition temperature between DIN and IMF pathways was about 225 K. At about 225 K, particles on S4 and S12 both took up water at 78% ± 2% and then formed ice upon further cooling. The subsequent ice nucleation of S12 could be homogeneous nucleation or IMF since the onset RH_{ice} of 150% ± 7% is close to the homogeneous nucleation limit. However, particles of S4 nucleated ice after water uptake through IMF at RH_{ice} of 140% ± 8% which is about 8% lower than the homogeneous nucleation limit. Below 225 K, particles of S4 and S12 nucleated ice via DIN at RH_{ice} from 133% ± 4% to 170% ± 8%. DIN occurred on the S11 particles at about 121% ± 3% to 130% ± 3% RH_{ice} below 225 K. S11 showed the lowest onset RH_{ice} among the investigated samples indicating that its ice nucleation efficiency was higher than other samples. The results of ice nucleation onset conditions for the investigated samples showed distinct variations in the ice nucleation ability for particles in the different marine atmospheres, even for the samples (S11, S12) with similar elemental composition and the dominant particle classes. The possible reasons for this are discussed in the later section.

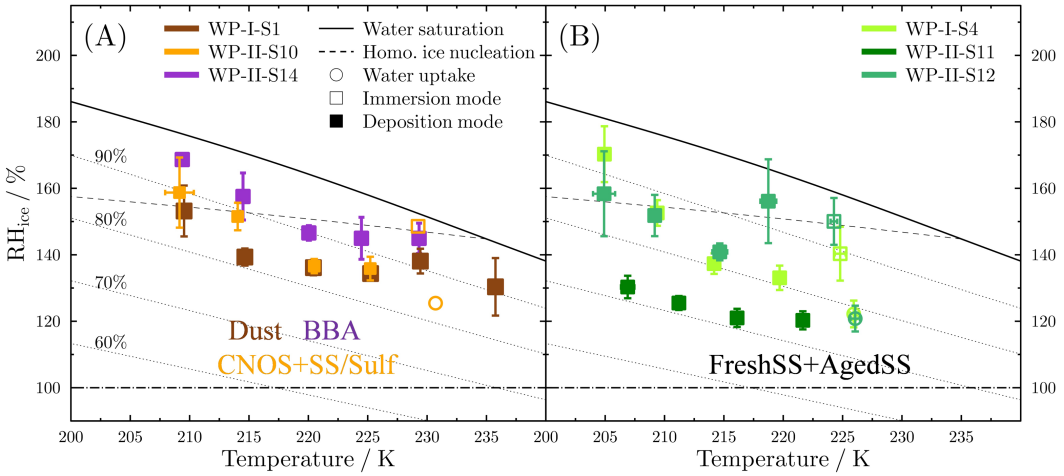

Figure 7. Onset conditions of freezing temperature and RH_{ice} for water uptake (open circles), immersion freezing (open squares), and deposition ice nucleation (solid squares) on particle samples. (**A**) Dust dominated sample (S1), BBA influenced sample (S14), and CNOS and SS/Sulf dominated

sample (S10); (B) FreshSS and AgedSS dominated samples (S4, S11, S12). Dashed line indicates the homogeneous freezing limits for aqueous droplets of 0.3 μm in diameter (Koop et al., 2000; Koop and Zobrist, 2009). Dotted lines represent different relative humidity (RH_w) shown in panel A. Solid and dased-dotted lines represent water saturation (100% RH_w) and ice saturation (100% RH_{ice}), respectively.

3.4 INP characterization

In total, 132 INPs together with 1317 non-INPs on the silicon wafer substrates were identified and characterized individually for their morphology and elemental composition. Figure 8 shows the representative SEM images and the corresponding EDX spectra of different types of INPs. SEM images for each identified INP at different temperatures are shown in Figs. S11, S12, and S13. The average ECD of INPs was generally greater than the ECD of the population considering both INPs and non-INPs together for each sample (Table 1). Of the 132 INPs, 71% of them were super-micron particles and the rest were submicron particles. The INPs exhibited different morphologies, such as crystalline irregular shapes (e.g., INPs classified as FreshSS, Aged SS, and Dust) and spherical shapes (e.g., INPs classified as CNOS). We found that the majority of INPs from S14 influenced by BBA had thick organic coatings (Fig. 8 and Fig. S11). The organic coating thickness of BBA INPs (1.07 ± 0.68 μm, n = 13) is significantly thicker than that of other BBA (0.53 ± 0.37 μm, n = 112) at the significant level of 0.001. Different number fractions of INPs identified in the FreshSS and AgedSS dominated samples (S4, S11, and S12) have organic coatings. More than 80% of INPs in S11 were coated with organics compared to S4 (33%) and S12 (30%). Figure S14 shows the elemental mapping of a representative INP with a thin organic coating. The mapping shows that Na and Cl were distributed in the core, while C and O were present throughout the whole 2-D projected area of this AgedSS INP. Previous studies have shown that solid organics can form ice via DIN at low temperatures (Wang et al., 2012b; Knopf et al., 2018; Lata et al., 2021; Alpert et al., 2022). We speculate that the organic coatings on the particles of S11 triggered the ice nucleation which have different ice nucleation abilities compared to S4 and S12.

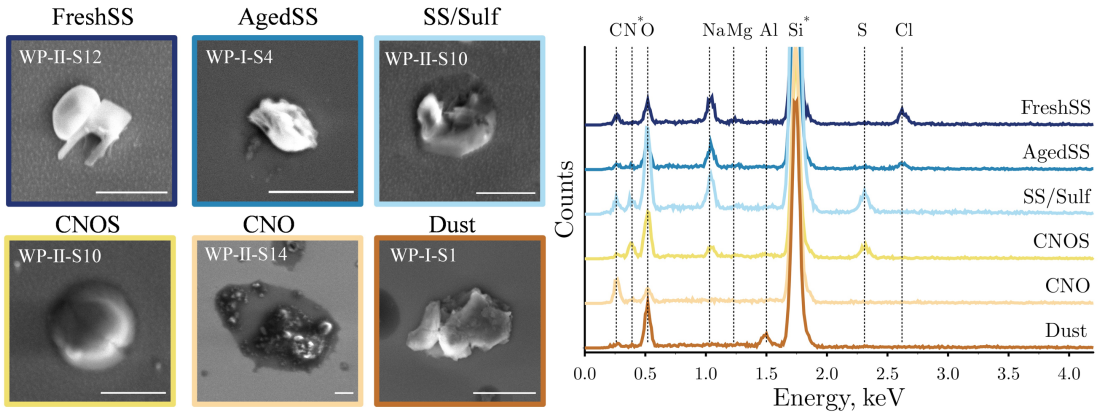

669

670 **Figure 8.** Representative SEM images and the corresponding EDX spectra for 6 classes of INPs.
671 The spectra include the substrate background signal of N and Si (asterisked) from silicon wafer
672 coated with Si_3N_4. Labels on SEM images are the name of samples. Scale bar is 2 μm for all images.

673

674 All the identified INPs and non-INPs on the substrates used in the ice nucleation
675 experiments were categorized based on the SEM/EDX data. Figure 9 shows the
676 percentages of different classes for INPs and the particle population in stacked bars
677 marked with "INPs" and "All", respectively. Taking S1 as an example, six particle
678 classes were identified in the particle population and the 19 identified INPs are from
679 five particle classes except for the CNO class. Similar to S1, the dominant particle
680 classes in the population of all respective samples are also the dominant classes of INPs.
681 This result suggests that all these major particle classes identified in our experiments
682 are potential INPs. We calculated the average elemental composition of INPs and non-
683 INPs for each particle type as shown in Fig. S15. A two-sample t-test was also
684 performed on the elemental compositions of INPs and non-INPs for each particle type.
685 At the significant level of 0.05, there is no sufficient evidence showing that the
686 elemental compositions of INPs and non-INPs are different. We also found that the
687 contributions of the same particle class in INPs and the particle population are different
688 in some cases. The most notable example is S10 where SS/Sulf particles contributed
689 77% of INPs, but only 51% of the population.

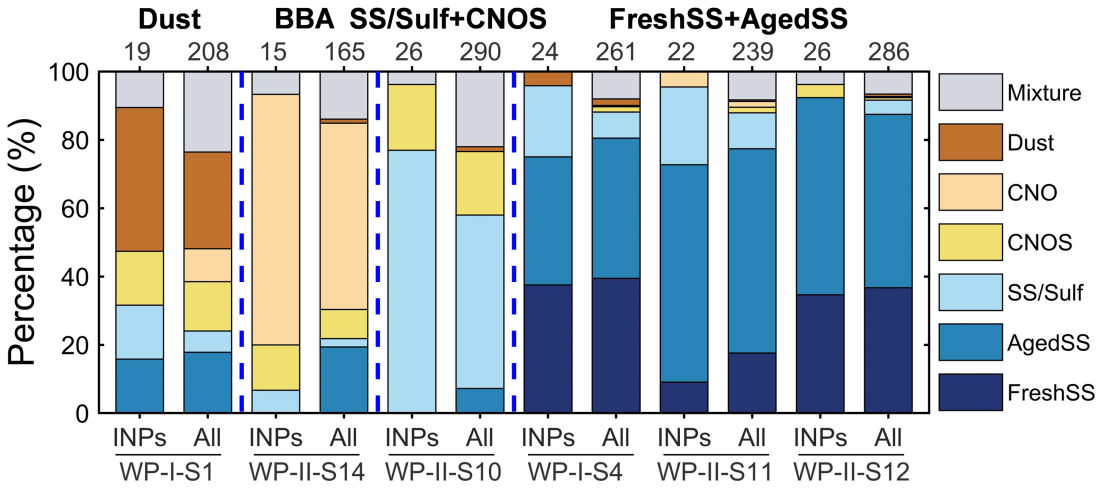

690

691 **Figure 9.** The number percentages of different particle classes for INPs and the particle population.
692 Data marked with "All" including both INPs and non-INPs. The corresponding numbers on the top
693 represent the investigated particle number. Blue dashed lines separate the samples with different
694 particle classes.

695

696 To further explore whether a particle class is unique when acting as INPs, we calculated
697 the enrichment factor (*EF*) for a given particle class (A) according to the following
698 formula:

699
$$EF(\mathrm{A}) = \frac{\left(\frac{N^{\mathrm{A}}_{\mathrm{INPs}}}{N_{\mathrm{INPs}}}\right)}{\left(\frac{N^{\mathrm{A}}_{\mathrm{INPs+non-INPs}}}{N_{\mathrm{INPs+non-INPs}}}\right)} \quad (14)$$

700 where N is the number of particles. *EF*(A) is the ratio of the contributions of the particle
701 class A in the INPs to the whole particle population (INPs + non-INPs). *EF* values of
702 each particle class for different samples are shown in Fig. 10. *EF* values with upper and
703 lower limits determined from Poisson distributed errors at 95% confidence level are
704 listed in Table S2. Although the enriched particle classes are diverse for different
705 samples, *EF* of the SS/Sulf class is greater than 1 for most of the samples except S12.
706 No INP was identified as SS/Sulf particle for S12 which only has 4% of SS/Sulf in the
707 population. The overall *EF* of the SS/Sulf class is 1.9 with the upper and lower limits
708 of 9.2 and 1.2, respectively. This indicates that the SS/Sulf particles were enriched in
709 INPs in these marine environments.

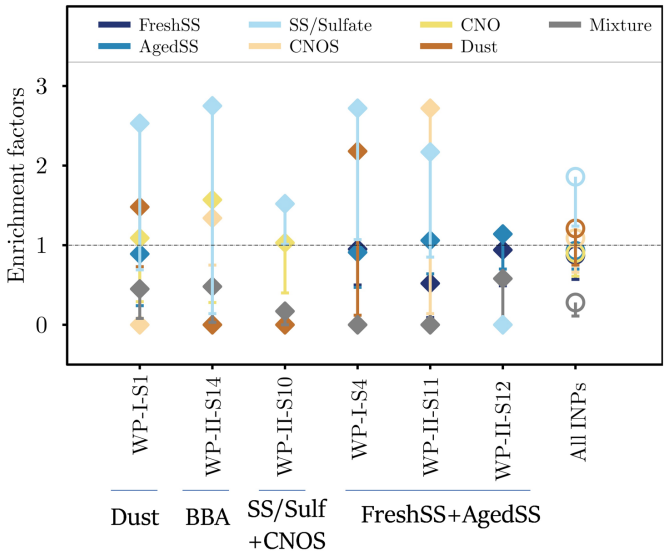

Figure 10. The *EF* of all INP classes for each sample (solid diamonds) and all INPs (open circles). The dashed line indicates *EF* of 1. The lower limits of *EF* were calculated by Poisson distribution at the confidence level of 95%. For the readability, the upper limits were not plotted here but the values are listed in Table S2.

3.5 Comparison of ice nucleation properties with previous studies

Figure 11 shows the comparison of ice nucleation data from our work and previous studies. The DIN onset conditions of the Dust dominated sample (S1) are similar to the feldspar between 230 K and 235 K (Yakobi-Hancock et al., 2013) and less efficient compared to bare dust particles, including montmorillonite (Welti et al., 2009; Kulkarni et al., 2014), illite (Welti et al., 2009; Kulkarni et al., 2014), quartz (Kulkarni et al., 2014), and kaolinite (Wang and Knopf, 2011). Previous laboratory studies showed that the aging processes can reduce the ice nucleation ability of mineral dust at temperatures relevant to cirrus clouds (Tang et al., 2016). For example, Primm et al. (2017) indicated that the ice nucleation ability of illite can be slightly suppressed by organic acids when mixed with a mixture of five dicarboxylic acids (referred to as M5) at an organic-illite mass ratio greater than 1:1. The DIN onset conditions of S1 are similar to the M5/illite (10:1) mixtures (Fig. 11A). We also found that coated particles (Fig. S16) in S1 serving as INPs have a similar coating thickness (Fig. S11) as organic coatings on M5/illite

730 greater than 1:1. Kulkarni et al. (2014) observed a decrease in ice nucleation ability of
731 montmorillonite, illite, and quartz at 235 K when coated with H_2SO_4. These H_2SO_4
732 coated dust particles had a similar onset RH_{ice} as compared to particles on S1 at 235 K.
733 During the cruise, S1 and S2 in the WP-I region were impacted by the dust storm
734 originating from western Asia. The dust particles were aged during the transport to the
735 coastal areas and some of them had clear coatings (Fig. S11 and Fig. S16). This is
736 consistent with the finding by Jang et al.(2023) from the same cruise that aerosol
737 particles in the S1 sample area have a high fraction of lignin-like organics. S1 had a
738 similar ice nucleation ability as dust particles with organic coatings. We suspect that the
739 ice nucleation efficiency of the dust particles at temperatures where DIN occurred on
740 the INP's surface was affected by coatings after aging.
741
742 Our results for S14 suggest that BBA from the Australian wildfires may have served as
743 INPs via DIN below 230 K. Combustion and burning processes produce a large number
744 of particles with mixed organic and inorganic components into the atmosphere (e.g.,
745 Fuzzi et al., 2007; Chen et al., 2017; Hodshire et al., 2019). Previous studies have shown
746 that soot, combustion ash, and BBA particles from different burning sources
747 demonstrated various ice nucleation properties (e.g., Jahl et al., 2021; Jahn et al., 2020;
748 Kanji et al., 2017 and references therein). Soot particles or their organic coatings on
749 S14 may have played a role in the observed ice nucleation events. Several studies have
750 reported that combustion related particles can serve as INPs via DIN below 233 K
751 (DeMott et al., 1999; Möhler et al., 2005a, b; Koehler et al., 2009; Kanji et al., 2011;
752 Chou et al., 2013). Kanji et al. (2011) showed the ice nucleation activated by soot
753 generated using a graphite spark generator (GSG) at about 145% RH_{ice}, a value similar
754 to S14 at 230 K. Chou et al. (2013) showed that wood burning particles nucleated ice
755 at about 136% RH_{ice} at about 233 K. DeMott et al. (1999) reported that the freezing
756 RH_{ice} of soot was close to the homogeneous freezing limits. S14 nucleated ice at higher
757 RH_{ice} than soot generated by GSG and particles containing organic carbon (Möhler et
758 al., 2005a, b), but lower than the soot studied by DeMott et al. (1999). Suwannee River
759 standard fulvic acid (SRFA) and leonardite were used as surrogates of atmospheric

organics from biomass burning (Wang and Knopf, 2011). Ice nucleation onset conditions of S14 are very similar to those of SRFA and ozone aged leonardite particles above 220 K but higher at lower temperatures.

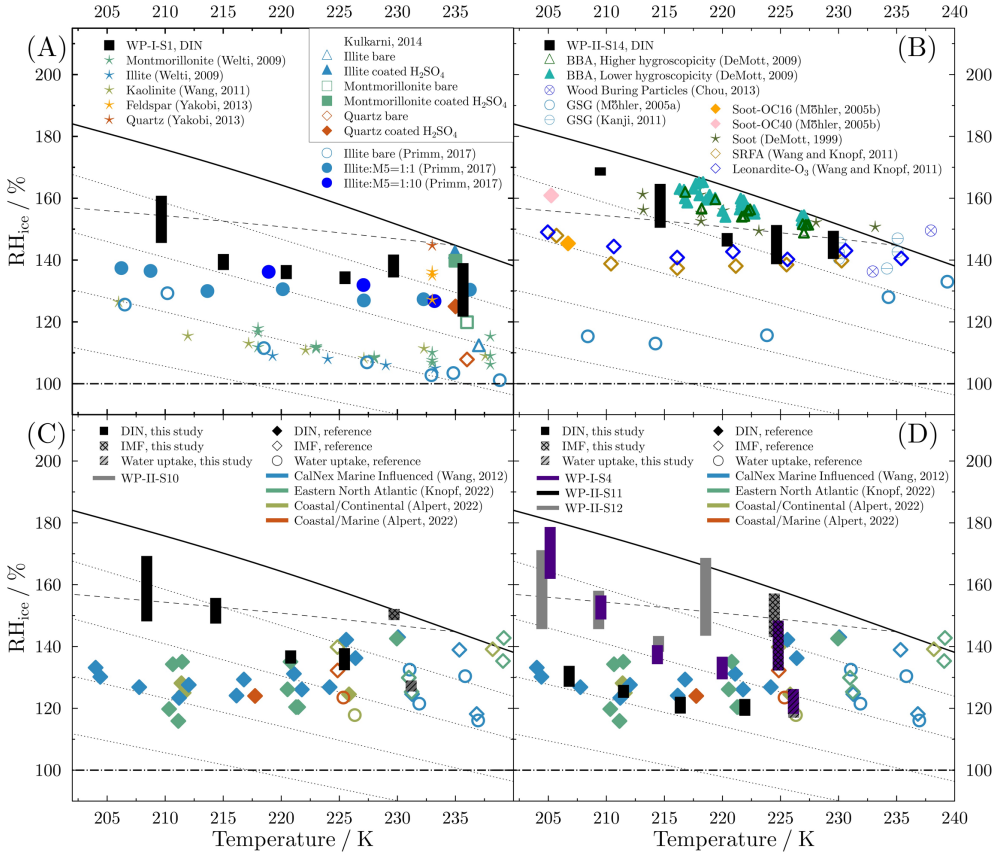

Figure 11. Ice nucleation and water uptake onset conditions (bars) for (A) Dust dominated sample (S1), (B) BBA influenced sample (S14), (C) CNOS and SS/Sulf dominated sample (S10), and (D) FreshSS and AgedSS dominated samples (S4, S11, S12) compared with previous studies (symbols) (DeMott et al., 1999, 2009; Möhler et al., 2005a, b; Welti et al., 2009; Kanji et al., 2011; Wang and Knopf, 2011; Wang et al., 2012a; Yakobi-Hancock et al., 2013; Kulkarni et al., 2014; Primm et al., 2017; Alpert et al., 2022; Knopf et al., 2022). Descriptions for the lines are the same as in Fig. 7.

Figures 11C and 11D show the comparison of data on marine related particles from previous studies with our data on sea salt containing particles. Several studies have shown that the aerosol particles collected in marine environments or coastal areas can act as efficient INPs at RH_{ice} between 115% and 143% (e.g., Wang et al., 2012a; Alpert et al., 2022; Knopf et al., 2022). Using the micro-spectroscopic analysis, these studies

identified the INPs and demonstrated that the major particle types in the population initiate ice formation. These particle types include the marine influenced particles with thin organic coatings collected during the CalNex field campaign (Wang et al., 2012a), the relatively fresh sea salt particles with marine-produced organics collected from the coast of Long Island, New York (Alpert et al., 2022), and the processed sea salt containing particles collected over the eastern North Atlantic (Knopf et al., 2022). There is one FreshSS and AgedSS dominated sample (S11) that nucleated ice at the same RH_{ice} onsets as compared to those marine-influenced particles from above mentioned studies. The other sea salt containing samples in this work including the CNOS and SS/Sulf dominated sample (S10) and the FreshSS and AgedSS dominated samples (S4, S12) showed very similar RH_{ice} onsets only at temperatures above 220 K but higher onsets below 220 K. The reason for this discrepancy at lower temperatures is not clear. Future work on the coating composition may provide more insight. Together with previous studies, we show that these marine influenced particles exhibit different ice nucleation efficiencies. These variations are likely contributed not only to the complex compositions but also to the physical and chemical mixing state of these particles.

3.6 Ice nucleation kinetics

Ice nucleation kinetic analysis was conducted using the experimental data, including the RH_{ice} and temperature onsets, particle surface area, number of nucleation events, and nucleation time. Classical nucleation theory (CNT) has been widely used in cloud models (e.g., Pruppacher and Klett, 2010; Khvorostyanov and Curry, 2004; Liu and Penner, 2005). In this study, heterogeneous ice nucleation rate coefficient (J_{het}), contact angle (θ), and their parameterizations are presented and discussed. Ice nucleation activated fraction of each sample was listed in Table 1 and discussed in Text S2. n_s based on the singular hypothesis (Vali, 1971; Connolly et al., 2009) and its parameterizations are also presented in Text S2.

3.6.1 Heterogeneous ice nucleation rate coefficient (J_{het})

According to CNT, ice nucleation is a stochastic process and continues with time, in contrast to the singular hypothesis (Pruppacher and Klett, 2010). J_{het} depends on temperature and RH_{ice}. J_{het} was derived following the approach in previous works (Wang and Knopf, 2011; Wang et al., 2012a; China et al., 2017; Knopf et al., 2022). Using the observed ice nucleation data, $J_{het} = N_{ice}/(t \times A_{tot})$, where N_{ice} is the number of the observed ice nucleation events that occurred in a temperature interval, A_{tot} is the total particle surface area available for ice nucleation experiment in the temperature interval, t of 6 seconds is the time interval between two consecutive OM images used to monitor ice formation. In the four groups of particle samples we investigated, J_{het} for DIN ranged from 130 to 1370 $cm^{-2}\ s^{-1}$, 40 to 2970 $cm^{-2}\ s^{-1}$, 40 to 1480 $cm^{-2}\ s^{-1}$, and 10 to 390 $cm^{-2}\ s^{-1}$ for the Dust dominated, BBA influenced, CNOS and SS/Sulf dominated, and FreshSS and AgedSS dominated samples, respectively. J_{het} for IMF ranged from 540 to 4780 $cm^{-2}\ s^{-1}$ for the FreshSS and AgedSS dominated samples.

3.6.2 Parameterizations of J_{het} and θ

The experimentally derived J_{het} was parameterized based on the water-activity-based approach. The water-activity-based approach has been widely used to describe the homogeneous ice nucleation of droplets and depends only on a droplet's water activity (a_w) and T_p (Koop et al., 2000). Homogeneous ice nucleation temperature follows a single curve as a function of a_w and is parameterized by a constant shift of a_w (i.e., Δa_w) from the ice melting temperature curve (Koop and Zobrist, 2009). This approach has also been applied to heterogeneous ice nucleation including DIN and IMF (Koop and Zobrist, 2009; Knopf and Alpert, 2013; China et al., 2017). It is assumed that particles were in equilibrium with the gas phase during the experiments, so $a_w = RH_w/100$. For each nucleation event, $\Delta a_w(T_f)$ is the difference between the RH_w at which ice nucleated and the RH_w on the ice melting curve at the observed ice nucleation temperature (T_f), or $a_w(T_f)$ and $a_w^{ice}(T_f)$, respectively. Then, $\Delta a_w(T_f) = a_w^{ice}(T_f) - a_w(T_f)$ (Knopf and Alpert, 2013; Koop and Zobrist, 2009), which can be calculated for each ice nucleation event using the ice nucleation onset temperature and RH_w. J_{het} was

calculated for all ice nucleation events and parameterized as a function of Δa_w following the previous works (China et al., 2017; Alpert et al., 2022; Knopf et al., 2022, 2023). Figure 12 presents the J_{het} (Δa_w) for the DIN and IMF data along with the parameterizations according to $\log(J_{het}) = c \times \Delta a_w + d$. The values of c and d parameters are listed in Table 2. The Dust dominated sample has higher J_{het} at the same Δa_w compared with the other samples. The BBA influenced sample only nucleated ice at higher Δa_w. The DIN J_{het} for the FreshSS and AgedSS samples changes by 2 orders of magnitude over a wide range of Δa_w. For the FreshSS and AgedSS samples, IMF J_{het} with a larger c displays a steeper slope than DIN J_{het}.

In Fig. 12, we compared our J_{het} parameterizations with previous studies. DIN J_{het} of the Dust-dominated sample is similar to the particles collected during the Aerosol and Cloud Experiments in the Eastern North Atlantic (ACE ENA) field campaign within the marine boundary layer (ACE ENA MBL) (Knopf et al., 2022, 2023). It is about 1-2 orders of magnitude lower than particles collected from the free troposphere (ACE ENA FT). DIN J_{het} of the other particle types investigated in this study are lower than particles collected from ACE ENA FT, ground site (ACE ENA GD), and ACE ENA MBL. This is consistent with the results showing that our particles nucleated ice at higher RH_{ice} than particles collected during ACE ENA (Fig. 11). DIN J_{het} for the FreshSS and AgedSS samples is similar to the SSA investigated by Alpert et al. (2022) in the lower Δa_w range (less than 0.25). This is likely because S11 nucleated ice in this Δa_w range (i.e., RH_{ice}) is similar to the SSA INP investigated by Alpert et al. (2022) as they have similar morphology and composition. IMF J_{het} of the FreshSS and AgedSS samples is slightly higher than particles from ACE ENA GD and 1-2 orders of magnitude higher than the other field samples (Fig. 12C). The IMF J_{het} of the FreshSS and AgedSS samples displays a smaller slope with Δa_w compared to the laboratory-generated particles, such as illite (Knopf and Alpert, 2013), natural dust (Alpert and Knopf, 2016; Niemand et al., 2012), leonardite particles (Knopf and Alpert, 2013), and diatomaceous material (Knopf and Alpert, 2013; Knopf et al., 2011; Alpert et al., 2011a, b). This is consistent with the study by Knopf et al. (2022) which suggested that the

diversity of ambient particles exhibit different ice nucleation efficiencies compared to single-component INP types studied in the laboratory at different temperature ranges. Our results emphasize the importance of studying the ice nucleation ability of particles and their parameterizations from different geological areas with different diversities in particle characteristics.

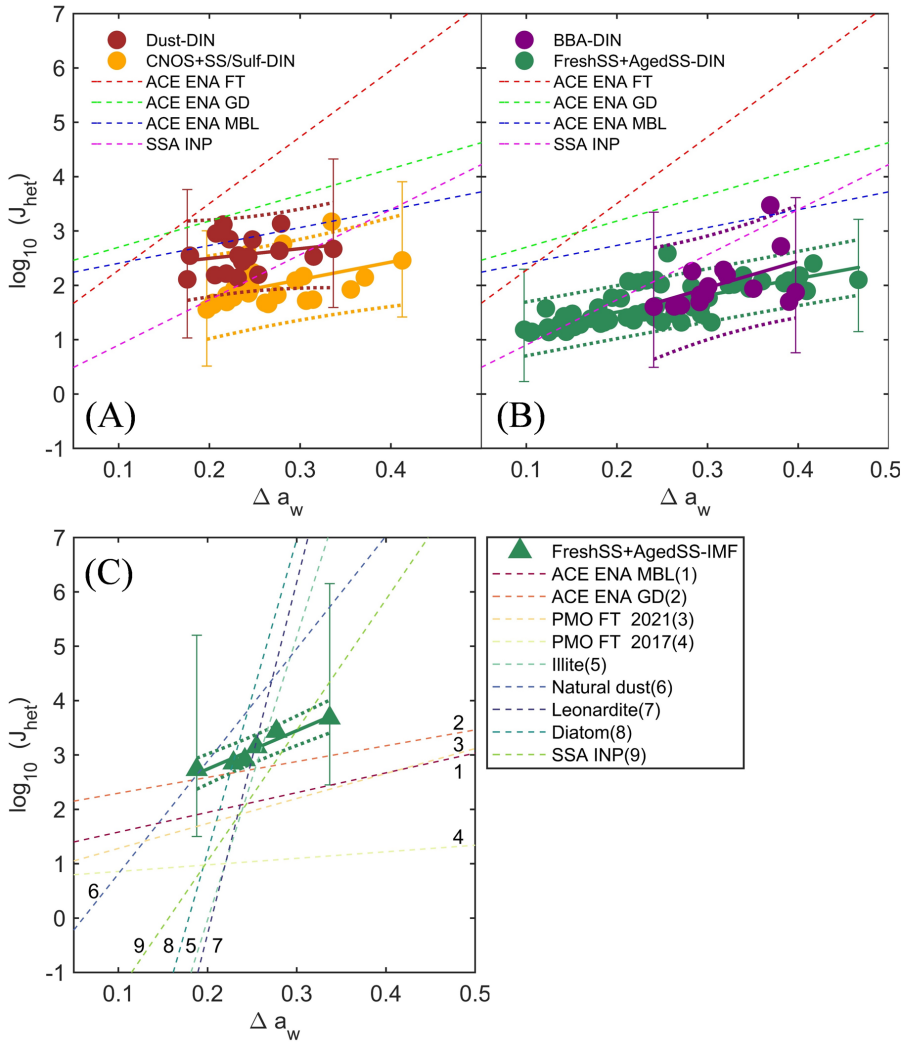

Figure 12. J_{het} as a function of Δa_w. Circles represent DIN J_{het} for (A) Dust, CNOS and SS/Sulf dominated samples, (B) BBA, FreshSS and AgedSS dominated samples. Triangles represent IMF J_{het} (C) for FreshSS and AgedSS dominated samples. Solid lines indicate the fittings according to $\log(J_{het}) = c \times \Delta a_w + d$ with associated dotted lines representing the 95% prediction intervals. Representative ΔJ_{het} (error bars) are plotted (Text S2). (A-B) Dashed red, green, and blue lines represent DIN J_{het} parameterizations of particles collected from ACE ENA FT (Knopf et al., 2023), ACE ENA GD (Knopf et al., 2022), and ACE ENA MBL (Knopf et al., 2023), respectively. Dashed

magenta line indicates J_{het} for SSA INPs (Alpert et al., 2022). (C) Dashed lines with the number label of 1-4 represent IMF J_{het} for particles from ACE ENA MBL (Knopf et al., 2023), ACE-ENA GD (Knopf et al., 2022), and the Pico Mountain Observatory (PMO) under free-tropospheric (FT) conditions in the Azores (PMO FT 2017 and PMO FT 2021) (China et al., 2017; Lata et al., 2021), respectively. Dashed lines with the number label of 5-8 represent IMF J_{het} for illite particles (Knopf and Alpert, 2013), natural dust (Alpert and Knopf, 2016; Niemand et al., 2012), leonardite particles (Knopf and Alpert, 2013), diatomaceous material (Diatom) (Knopf and Alpert, 2013; Knopf et al., 2011; Alpert et al., 2011a, b), and SSA INP (Alpert et al., 2022), respectively.

Table 2 The c and d values for the parameterizations of J_{het} as a function of Δa_w,

$$\log(J_{\mathrm{het}}) = c \times \Delta a_{\mathrm{w}} + d.$$

Sample type	c	LCL_c	UCL_c	d	LCL_d	UCL_d	RMSE
Dust-DIN	1.78	– 0.15	3.72	2.14	1.67	2.61	0.31
BBA-DIN	4.88	2.38	7.39	0.49	– 0.31	1.30	0.43
CNOS+SS/Sulf-DIN	3.24	1.91	4.57	1.13	0.77	1.50	0.35
FreshSS+AgedSS-DIN	3.09	2.76	3.42	0.89	0.81	0.97	0.24
FreshSS+AgedSS-IMF	7.06	6.03	8.09	1.33	1.06	1.60	0.09

θ for DIN is derived based on CNT following our previous studies (Wang and Knopf, 2011; Wang et al., 2012a). θ is calculated from J_{het} and the ice nucleation onset temperature and RH_{ice} using the following formula: $J_{\mathrm{het}} = \mathrm{A} \times \exp\left(\frac{-\Delta F_{\mathrm{g,het}}}{kT}\right)$, where A is a pre-exponential factor and k is the Boltzmann constant. $\Delta F_{\mathrm{g,het}}$ is the free energy of ice embryo formation, which is defined as $\Delta F_{\mathrm{g,het}} = \frac{16\pi M_{\mathrm{w}}^2 \sigma_{\mathrm{i/v}}^3}{3[RT\rho \ln S_{\mathrm{ice}}]^2} \times f(m)$, where R is the universal gas constant, ρ is the density of ice, S_{ice} is the ice saturation ratio ($S_{\mathrm{ice}} = RH_{\mathrm{ice}}/100\%$), M_{w} is the water molecular weight, $\sigma_{\mathrm{i/v}}$ is the surface tension at the ice-vapor interface. $f(m)$ is the geometric factor and is defined as $f(m) = (m^3 - 3m + 2)/4$, where $m = \cos(\theta)$. A smaller value of θ implies higher ice nucleation efficiency and should translate to relatively lower RH_{ice} onsets in our experiments. Figure 13 represents the mean θ as a function of temperature for INPs of all sample types. When comparing θ at the same temperature, the FreshSS and AgedSS dominated samples, in general, have the smallest θ, followed by the Dust dominated, CNOS and SS/Sulf

dominated, and BBA influenced samples. For all the investigated samples, θ was relatively constant above 220 K and increased as temperature decreased to 205 K. We propose new parameterizations of θ as a function of $T^3\ln[RH_{\mathrm{ice}}]^2$ (Text S2). θ for various particle types fall tightly into the parameterization as shown in Fig. S19.

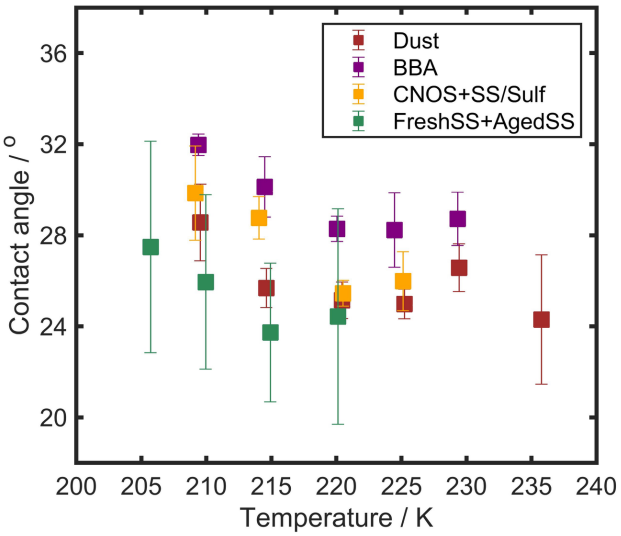

Figure 13. Mean values with one standard deviations of contact angle for DIN by the Dust, BBA, CNOS and SS/Sulf, FreshSS and AgedSS dominated samples.

3.7 Ice nucleation propensity and mixing state of particle population

Previous studies have used χ to estimate the error in predicting aerosol CCN activity and optical properties when assuming idealized mixing states (Ching et al., 2017; Yao et al., 2022). For example, Ching et al. (2017) quantified the error in predicting CCN concentration as a function of χ. When internal mixing was assumed, errors of up to 100% overpredicting CCN concentration were found for populations with more external mixing (χ < 60%). However, CCN concentrations were well predicted for populations with χ > 75%. Inspired by these studies, we used θ as a measure of particle ice nucleation propensity to discuss the potential link between the mixed state of population and particle ice nucleation propensity. We investigated the relative difference (error) in θ for the field samples compared to pure NaCl particles. Ice nucleation experiments were conducted on the laboratory-generated NaCl particles (Text S3) and θ was calculated for NaCl particles (see Section 3.6.2 for the calculation

924 details). Pure NaCl particles were used as a surrogate of complete internally mixed
925 marine aerosols (χ = 100%). We analyzed the relationship between the relative error in
926 θ of INPs (*Err*) and the mixing state of the population in which the INPs were identified.
927 *Err* of each INP from a field sample with a given mixing state (χ) was defined as:

928 $$Err = \frac{\theta(\chi) - \theta(100\%)}{\theta(100\%)} \times 100 \quad (15)$$

929 where $\theta(100\%)$ is the average θ for the NaCl standard. As shown in Fig. 14, χ for the
930 six investigated samples changed from 61% to 86%. Five samples (S1, S4, S10, S12,
931 and S14) exhibited positive mean *Err* ranging from 2.3% ± 7.5% to 16.3% ± 6.6%,
932 while S11 had a negative mean *Err* of -18.6% ± 6.2%. The FreshSS and AgedSS
933 dominated samples, S4 and S12, have a mean *Err* of 6.9% ± 12.4% and 13.0% ± 9.2%,
934 respectively.
935
936 The θ for particles in the marine environment is different from that for NaCl particles.
937 This can lead to errors in J_{het} of several orders of magnitude if the model assumes an
938 internally mixed particle population. According to CNT, we calculated DIN J_{het} for
939 NaCl and particles with *Err* of 5% and 10% under different temperature and humidity
940 conditions (Fig. S20). Between 135% and 180% RH_{ice}, *Err* of 5% and 10% will result
941 in 1.5 – 4 and 2 – 10 orders of magnitude differences in J_{het}, respectively. Moreover,
942 the lower the temperature and RH_{ice}, the larger the error in J_{het}. This suggests that the
943 effects of aging processes and mixing state need to be considered in the ice nucleation
944 modeling. No specific correlation or trend was found between χ and the *Err* from this
945 data set with the limited number of samples. This may be expected since ice nucleation
946 is controlled by various physiochemical properties of individual particles, particularly
947 for DIN. For example, one crucial factor is the physical mixing state of particle, such
948 as coating. Organic coatings play a significant role in altering the θ of sea salt particles,
949 as exemplified by S11 compared to S4 and S12. In contrast to CCN, which in general
950 can be described by the κ-Köhler theory, there are still no appropriate physical models
951 to describe INPs. In addition, ice nucleation propensity for DIN is determined on the
952 individual particle basis, whereas the chemical mixing state (i.e., χ here) characterizes

the overall mixing of species within the particle population. There is a large gap in the understanding of the relationship between INP propensity and χ.

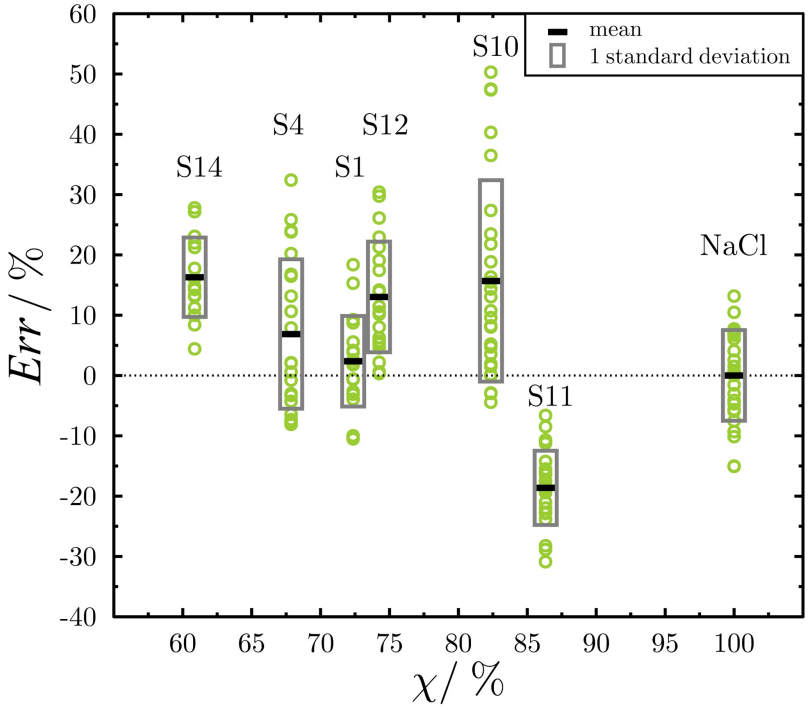

Figure 14. *Err* in θ for the investigated samples relative to the internally mixed particles (pure NaCl particles, χ = 100%). Black thick lines indicate the average θ and the gray boxes represent one standard deviation. Green circles represent θ for individual INPs.

4 Atmospheric implications

We found that the distinct mixing states of particle populations were affected by several processes over different oceans. In the marine atmosphere that already has a contribution of sea salt particles, adding more fresh sea salt particles makes the population more internally mixed (Fig. 6). We suspect that over open oceans where sea salt particle flux is large, the population will be mostly internally mixed. The addition of new particle types from other sources, such as dust storms (WP-I, S1, S2), biomass burning (WP-II, S14, S15), and secondary sources (CNOS in the SO region), will decrease the mixing state index and the population will become more externally mixed. These results are consistent with the proposed schematic description by Riemer et al. (2019) on the evolution of particle mixing state. We showed that multiphase processes

lead to the aging of fresh sea salt particles resulting in chlorine deficiency and thus changing the mixing state of the population (Fig. 5). This is a selective process that occurred on the sea salt particles and is different from the aging by condensation of secondary materials. As discussed in Section 3.2, these types of selective or inhomogeneous aging on particles move the population toward a more externally mixed state. To the best of our knowledge, this is not considered in the models predicting the mixing state of aerosols, even for the particle-resolved model. Our study suggests that, when discussing the influence of aging on the evolution of the mixing state, it is necessary to consider whether the aging processes occur uniformly on all particles.

We characterized chemical compositions for particle population and INPs at the single particle level. We found that all the identified particle types from different sources have the potential to serve as INPs, but have different ice nucleation efficiencies (Fig. 7 and Fig. 9). We found that S11 showed the highest ice nucleation efficiency among the FreshSS and AgedSS dominated samples (Fig. 7), which we attributed to the organic coatings on the particles. This indicates the importance of characterizing the physical mixing state of particles (i.e., morphology). INPs were enriched in SS/Sulf class, suggesting that the aging process alters ice nucleation ability by changing the chemical mixing state of particles. Considering the characterizations of individual particles and INPs, the ice nucleation onset conditions, and the derived freezing kinetics, it is suggested that the ice nucleation abilities at cirrus conditions of these complex marine aerosols are affected not only by the particle compositions but also by the mixing state of particle population. Future investigations on how the chemical and physical mixing state of particles affects ice nucleation in the atmosphere are needed for a better understanding of aerosol-cloud interactions in the climate system.

According to the singular hypothesis and CNT, ice nucleation kinetic parameters, J_{het} and n_s, were derived from the experimental data. We derived parameterizations of n_s as a function of temperature for IMF and DIN of different dominated particle classes. We also proposed parameterizations of J_{het} as a function of Δa_w for IMF and DIN based on

the water-activity based theory. In addition, θ was derived for DIN based on CNT. We propose new parameterizations of θ that take into account both temperature and RH_{ice}. These parameterizations can be used to estimate the INP concentrations or ice crystal production rates when particle surface area data are available. These parameterizations can be used in cloud models with different ice nucleation descriptions to evaluate the potential sources and impacts of different particles on cloud formation in the marine atmosphere.

5 Conclusions

Composition, mixing state, and ice nucleation properties were investigated for the aerosol particles collected over the Western Pacific and Southern Ocean during a cruise from South Korea (34.93°N) to the Ross Sea (75.12°S) in 2019. Seven particle classes were identified including fresh sea salt, aged sea salt, sea salt mixed with sulfate, carbonaceous particle, sulfur-containing particle, dust, and mixture. Contributions of these particles varied across oceans at different latitudes. Except for the samples impacted by dust storm, fresh sea salt, aged sea salt, and sea salt mixed with sulfate particles were the most prevalent particle types with the total number percentage ranging from 48% to 99%. Particles showed different degrees of chloride depletion due to the aging processes of acid displacements on sea salt particles. Significant contributions of sulfur-containing particles up to 93% in number were found in the Ross Sea, which was affected by phytoplankton blooms in the austral summer. The chemical mixing state index of particle population ranges from 50% to 95%. The mixing state index was positively correlated with the number percentages of fresh sea salt and negatively correlated with the proportion of sulfur-containing particles. Particle populations tended to be more internally mixed as the fresh sea salt fraction increased. When sea salt particles were a background or dominant particle type, inhomogeneous aging processes and new particle sources made the population more externally mixed.

We showed that different types of particle samples demonstrated a variety of ice

nucleation abilities at cirrus conditions. The sample dominated by the fresh sea salt particles with organic coatings exhibited the highest ice nucleation efficiency with RH_{ice} onset as low as 121%, while particles influenced by biomass burning were the least efficient among the investigated samples. According to the individual INP characterizations, the dominant particle types in the population all contribute to the identified INPs but with different enrichment factors. The sea salt mixed with sulfate particles were enriched in INPs with an overall factor of about 1.9. Ice nucleation abilities of marine aerosol particles were affected not only by composition but also by the chemical and physical mixing state of the particle population. Ice nucleation kinetic parameters, time-dependent J_{het}, time-independent n_s, and contact angle, were derived from the experimental data. The corresponding parameterizations for different particle types are provided for cloud modeling. In this study, we demonstrated the diversity in the particle characteristics at the single particle level, the mixing state of particle population, and particles' abilities to form ice crystals in different marine atmospheres in both the northern and southern hemispheres. The results motivate the need for further investigations of how the mixing state of particles affects ice nucleation in the atmosphere.

Data availability. All data are given in the main text or in the Supplement. HYSPLIT data were obtained through the NOAA website (https://www.ready.noaa.gov/hypub-bin/trajasrc.pl). NAAPS aerosol reanalysis data were obtained from https://nrlgodae1.nrlmry.navy.mil/ftp/outgoing/nrl/NAAPS-REANALYSIS/. FIRMS data were obtained from https://firms.modaps.eosdis.nasa.gov/.

Supplement. The supplement related to this article is available online.

Author contributions. XJ performed the experiments and wrote the first draft of the manuscript. XJ, TZ, JP, and BW performed the data analysis. JP and KP collected the samples. BW, JP and KP initiated and designed the study. BW supervised the

project. BW, YJY, and XJ led the discussion and all authors contributed to the data interpretation and the manuscript writing.

Competing interests. The authors declare that they have no conflict of interest.

Acknowledgements. BW, XJ, and TZ thank the support by National Science Foundation of China (42075076, 41775133), Fundamental Research Funds for the Central Universities (20720160111, 20720190147). This study is also partially funded by the Korea Polar Research Institute research grant (PE23110, PE23030). BW and JY thank the support by the Fund of Key Laboratory of Global Change and Marine-Atmospheric Chemistry, MNR (GCMAC2004). TZ acknowledges the support by the PhD Fellowship of the State Key Laboratory of Marine Environmental Science at Xiamen University. We thank the staff onboard R/V *Araon* helping the sampling during the Antarctic cruise and Peter A. Alpert for helpful discussion and manuscript revision.

References

Adachi, K., Oshima, N., Gong, Z., de Sá, S., Bateman, A. P., Martin, S. T., de Brito, J. F., Artaxo, P., Cirino, G. G., Sedlacek III, A. J., and Buseck, P. R.: Mixing states of Amazon basin aerosol particles transported over long distances using transmission electron microscopy, Atmos. Chem. Phys., 20, 11923–11939, https://doi.org/10.5194/acp-20-11923-2020, 2020.

Alpert, P. A. and Knopf, D. A.: Analysis of isothermal and cooling-rate-dependent immersion freezing by a unifying stochastic ice nucleation model, Atmos. Chem. Phys., 16, 2083–2107, https://doi.org/10.5194/acp-16-2083-2016, 2016.

Alpert, P. A., Aller, J. Y., and Knopf, D. A.: Ice nucleation from aqueous NaCl droplets with and without marine diatoms, Atmos. Chem. Phys., 11, 5539–5555, https://doi.org/10.5194/acp-11-5539-2011, 2011a.

Alpert, P. A., Aller, J. Y., and Knopf, D. A.: Initiation of the ice phase by marine biogenic surfaces in supersaturated gas and supercooled aqueous phases, Phys. Chem. Chem. Phys., 13, 19882, https://doi.org/10.1039/c1cp21844a, 2011b.

Alpert, P. A., Kilthau, W. P., O' Brien, R. E., Moffet, R. C., Gilles, M. K., Wang, B., Laskin, A., Aller, J. Y., and Knopf, D. A.: Ice-nucleating agents in sea spray aerosol identified and quantified

with a holistic multimodal freezing model, Sci. Adv., 8, 1–11, https://doi.org/10.1126/sciadv.abq6842, 2022.

Angle, K. J., Crocker, D. R., Simpson, R. M. C., Mayer, K. J., Garofalo, L. A., Moore, A. N., Mora Garcia, S. L., Or, V. W., Srinivasan, S., Farhan, M., Sauer, J. S., Lee, C., Pothier, M. A., Farmer, D. K., Martz, T. R., Bertram, T. H., Cappa, C. D., Prather, K. A., and Grassian, V. H.: Acidity across the interface from the ocean surface to sea spray aerosol, Proc. Natl. Acad. Sci., 118, 1–6, https://doi.org/10.1073/pnas.2018397118, 2021.

Ault, A. P., Moore, M. J., Furutani, H., and Prather, K. A.: Impact of emissions from the Los Angeles Port Region on San Diego air quality during regional transport events, Environ. Sci. Technol., 43, 3500–3506, https://doi.org/10/d7kt9s, 2009.

Ault, A. P., Gaston, C. J., Wang, Y., Dominguez, G., Thiemens, M. H., and Prather, K. A.: Characterization of the single particle mixing state of individual ship plume events measured at the Port of Los Angeles, Environ. Sci. Technol., 44, 1954–1961, https://doi.org/10.1021/es902985h, 2010.

Baccarini, A., Dommen, J., Lehtipalo, K., Henning, S., Modini, R. L., Gysel-Beer, M., Baltensperger, U., and Schmale, J.: Low-volatility vapors and new particle formation over the Southern Ocean during the Antarctic circumnavigation expedition, J. Geophys. Res.: Atmos., 126, https://doi.org/10.1029/2021JD035126, 2021.

Barnes, I., Hjorth, J., and Mihalopoulos, N.: Dimethyl sulfide and dimethyl sulfoxide and their oxidation in the atmosphere, Chem. Rev., 106, 940–975, https://doi.org/10.1021/cr020529+, 2006.

Beck, L. J., Sarnela, N., Junninen, H., Hoppe, C. J. M., Garmash, O., Bianchi, F., Riva, M., Rose, C., Peräkylä, O., Wimmer, D., Kausiala, O., Jokinen, T., Ahonen, L., Mikkilä, J., Hakala, J., He, X., Kontkanen, J., Wolf, K. K. E., Cappelletti, D., Mazzola, M., Traversi, R., Petroselli, C., Viola, A. P., Vitale, V., Lange, R., Massling, A., Nøjgaard, J. K., Krejci, R., Karlsson, L., Zieger, P., Jang, S., Lee, K., Vakkari, V., Lampilahti, J., Thakur, R. C., Leino, K., Kangasluoma, J., Duplissy, E., Siivola, E., Marbouti, M., Tham, Y. J., Saiz-Lopez, A., Petäjä, T., Ehn, M., Worsnop, D. R., Skov, H., Kulmala, M., Kerminen, V., and Sipilä, M.: Differing mechanisms of new particle formation at two Arctic sites, Geophys. Res. Lett., 48, 1–11, https://doi.org/10/gjrb6h, 2021.

Berndt, T., Hoffmann, E. H., Tilgner, A., Stratmann, F., and Herrmann, H.: Direct sulfuric acid formation from the gas-phase oxidation of reduced-sulfur compounds, Nat. Commun., 14, 4849, https://doi.org/10/gs3whz, 2023.

Brean, J., Dall' Osto, M., Simó, R., Shi, Z., Beddows, D. C. S., and Harrison, R. M.: Open ocean and coastal new particle formation from sulfuric acid and amines around the Antarctic Peninsula, Nat. Geosci., 14, 383–388, https://doi.org/10.1038/s41561-021-00751-y, 2021.

Burrows, S. M., McCluskey, C. S., Cornwell, G., Steinke, I., Zhang, K., Zhao, B., Zawadowicz, M., Raman, A., Kulkarni, G., China, S., Zelenyuk, A., and DeMott, P. J.: Ice-nucleating particles that

impact clouds and climate: observational and modeling research needs, Rev. Geophys., 60, 1–45, https://doi.org/10/gs6w5x, 2022.

Charnawskas, J. C., Alpert, P. A., Lambe, A. T., Berkemeier, T., O' Brien, R. E., Massoli, P., Onasch, T. B., Shiraiwa, M., Moffet, R. C., Gilles, M. K., Davidovits, P., Worsnop, D. R., and Knopf, D. A.: Condensed-phase biogenic-anthropogenic interactions with implications for cold cloud formation, Faraday Discuss., 200, 165–194, https://doi.org/10.1039/C7FD00010C, 2017.

Chen, J., Li, C., Ristovski, Z., Milic, A., Gu, Y., Islam, M. S., Wang, S., Hao, J., Zhang, H., He, C., Guo, H., Fu, H., Miljevic, B., Morawska, L., Thai, P., Lam, Y. F., Pereira, G., Ding, A., Huang, X., and Dumka, U. C.: A review of biomass burning: Emissions and impacts on air quality, health and climate in China, Sci. Total Environ., 579, 1000–1034, https://doi.org/10.1016/j.scitotenv.2016.11.025, 2017.

Chen, Q., Sherwen, T., Evans, M., and Alexander, B.: DMS oxidation and sulfur aerosol formation in the marine troposphere: a focus on reactive halogen and multiphase chemistry, Atmos. Chem. Phys., 18, 13617–13637, https://doi.org/10.5194/acp-18-13617-2018, 2018.

China, S., Alpert, P. A., Zhang, B., Schum, S., Dzepina, K., Wright, K., Owen, R. C., Fialho, P., Mazzoleni, L. R., Mazzoleni, C., and Knopf, D. A.: Ice cloud formation potential by free tropospheric particles from long-range transport over the Northern Atlantic Ocean, J. Geophys. Res.: Atmos., 122, 3065–3079, https://doi.org/10.1002/2016JD025817, 2017.

China, S., Burrows, S. M., Wang, B., Harder, T. H., Weis, J., Tanarhte, M., Rizzo, L. V., Brito, J., Cirino, G. G., Ma, P.-L., Cliff, J., Artaxo, P., Gilles, M. K., and Laskin, A.: Fungal spores as a source of sodium salt particles in the Amazon basin, Nat. Commun., 9, 4793, https://doi.org/10.1038/s41467-018-07066-4, 2018.

Ching, J., Fast, J., West, M., and Riemer, N.: Metrics to quantify the importance of mixing state for CCN activity, Atmos. Chem. Phys., 17, 7445–7458, https://doi.org/10.5194/acp-17-7445-2017, 2017.

Chou, C., Kanji, Z. A., Stetzer, O., Tritscher, T., Chirico, R., Heringa, M. F., Weingartner, E., Prévôt, A. S. H., Baltensperger, U., and Lohmann, U.: Effect of photochemical ageing on the ice nucleation properties of diesel and wood burning particles, Atmos. Chem. Phys., 13, 761–772, https://doi.org/10.5194/acp-13-761-2013, 2013.

Cochran, R. E., Ryder, O. S., Grassian, V. H., and Prather, K. A.: Sea spray aerosol: The chemical link between the oceans, atmosphere, and climate, Acc. Chem. Res., 50, 599–604, https://doi.org/10.1021/acs.accounts.6b00603, 2017.

Connolly, P. J., Möhler, O., Field, P. R., Saathoff, H., Burgess, R., Choularton, T., and Gallagher, M.: Studies of heterogeneous freezing by three different desert dust samples, Atmos. Chem. Phys., 9, 2805–2824, https://doi.org/10/bhhzwn, 2009.

Cornwell, G. C., McCluskey, C. S., Levin, E. J. T., Suski, K. J., DeMott, P. J., Kreidenweis, S. M., and Prather, K. A.: Direct online mass spectrometry measurements of ice nucleating particles

at a California coastal site, J. Geophys. Res.: Atmos., 124, 12157–12172, https://doi.org/10.1029/2019JD030466, 2019.

Cziczo, D. J., Ladino, L., Boose, Y., Kanji, Z. A., Kupiszewski, P., Lance, S., Mertes, S., and Wex, H.: Measurements of ice nucleating particles and ice residuals, Meteorol. Monogr., 58, 8.1-8.13, https://doi.org/10.1175/AMSMONOGRAPHS-D-16-0008.1, 2017.

De Leeuw, G., Andreas, E. L., Anguelova, M. D., Fairall, C. W., Lewis, E. R., O' Dowd, C., Schulz, M., and Schwartz, S. E.: Production flux of sea spray aerosol, Rev. Geophys., 49, 1–39, https://doi.org/10.1029/2010RG000349, 2011.

DeMott, P. J., Chen, Y., Kreidenweis, S. M., Rogers, D. C., and Sherman, D. E.: Ice formation by black carbon particles, Geophys. Res. Lett., 26, 2429–2432, https://doi.org/10.1029/1999GL900580, 1999.

DeMott, P. J., Petters, M. D., Prenni, A. J., Carrico, C. M., Kreidenweis, S. M., Collett, J. L., and Moosmüller, H.: Ice nucleation behavior of biomass combustion particles at cirrus temperatures, J. Geophys. Res.: Atmos., 114, 1–13, https://doi.org/10.1029/2009JD012036, 2009.

DeMott, P. J., Hill, T. C. J., McCluskey, C. S., Prather, K. A., Collins, D. B., Sullivan, R. C., Ruppel, M. J., Mason, R. H., Irish, V. E., Lee, T., Hwang, C. Y., Rhee, T. S., Snider, J. R., McMeeking, G. R., Dhaniyala, S., Lewis, E. R., Wentzell, J. J. B., Abbatt, J., Lee, C., Sultana, C. M., Ault, A. P., Axson, J. L., Diaz Martinez, M., Venero, I., Santos-Figueroa, G., Stokes, M. D., Deane, G. B., Mayol-Bracero, O. L., Grassian, V. H., Bertram, T. H., Bertram, A. K., Moffett, B. F., and Franc, G. D.: Sea spray aerosol as a unique source of ice nucleating particles, Proc. Natl. Acad. Sci. U.S.A., 113, 5797–5803, https://doi.org/10.1073/pnas.1514034112, 2016.

Ditas, J., Ma, N., Zhang, Y., Assmann, D., Neumaier, M., Riede, H., Karu, E., Williams, J., Scharffe, D., Wang, Q., Saturno, J., Schwarz, J. P., Katich, J. M., McMeeking, G. R., Zahn, A., Hermann, M., Brenninkmeijer, C. A. M., Andreae, M. O., Pöschl, U., Su, H., and Cheng, Y.: Strong impact of wildfires on the abundance and aging of black carbon in the lowermost stratosphere, Proc. Natl. Acad. Sci., 115, E11595–E11603, https://doi.org/10.1073/pnas.1806868115, 2018.

Ervens, B., Sorooshian, A., Aldhaif, A. M., Shingler, T., Crosbie, E., Ziemba, L., Campuzano-Jost, P., Jimenez, J. L., and Wisthaler, A.: Is there an aerosol signature of chemical cloud processing?, Atmos. Chem. Phys., 18, 16099–16119, https://doi.org/10.5194/acp-18-16099-2018, 2018.

Fraund, M., Pham, D., Bonanno, D., Harder, T., Wang, B., Brito, J., de Sá, S., Carbone, S., China, S., Artaxo, P., Martin, S., Pöhlker, C., Andreae, M., Laskin, A., Gilles, M., and Moffet, R.: Elemental mixing state of aerosol particles collected in central Amazonia during GoAmazon2014/15, Atmosphere, 8, 1–27, https://doi.org/10.3390/atmos8090173, 2017.

Fu, P. Q., Kawamura, K., Chen, J., Charrière, B., and Sempéré, R.: Organic molecular composition of marine aerosols over the Arctic Ocean in summer: Contributions of primary emission and secondary aerosol formation, Biogeosciences, 10, 653–667,

https://doi.org/10.5194/bg-10-653-2013, 2013.

Fuzzi, S., Decesari, S., Facchini, M. C., Cavalli, F., Emblico, L., Mircea, M., Andreae, M. O., Trebs, I., Hoffer, A., Guyon, P., Artaxo, P., Rizzo, L. V., Lara, L. L., Pauliquevis, T., Maenhaut, W., Raes, N., Chi, X., Mayol-Bracero, O. L., Soto-García, L. L., Claeys, M., Kourtchev, I., Rissler, J., Swietlicki, E., Tagliavini, E., Schkolnik, G., Falkovich, A. H., Rudich, Y., Fisch, G., and Gatti, L. V.: Overview of the inorganic and organic composition of size-segregated aerosol in Rondônia, Brazil, from the biomass-burning period to the onset of the wet season, J. Geophys. Res.: Atmos., 112, 1–35, https://doi.org/10.1029/2005JD006741, 2007.

Geng, X., Zhong, G., Li, J., Cheng, Z., Mo, Y., Mao, S., Su, T., Jiang, H., Ni, K., and Zhang, G.: Molecular marker study of aerosols in the northern South China Sea: Impact of atmospheric outflow from the Indo-China Peninsula and South China, Atmos. Environ., 206, 225–236, https://doi.org/10.1016/j.atmosenv.2019.02.033, 2019.

Han, Y., Fang, X., Xi, X., Song, L., and Yang, S.: Dust storm in Asia continent and its bio-environmental effects in the North Pacific: A case study of the strongest dust event in April, 2001 in central Asia, Sci. Bull., 51, 723–730, https://doi.org/10.1007/s11434-006-0723-2, 2006.

Healy, R. M., Sciare, J., Poulain, L., Crippa, M., Wiedensohler, A., Prévôt, A. S. H., Baltensperger, U., Sarda-Estève, R., McGuire, M. L., Jeong, C.-H., McGillicuddy, E., O' Connor, I. P., Sodeau, J. R., Evans, G. J., and Wenger, J. C.: Quantitative determination of carbonaceous particle mixing state in Paris using single-particle mass spectrometer and aerosol mass spectrometer measurements, Atmos. Chem. Phys., 13, 9479–9496, https://doi.org/10.5194/acp-13-9479-2013, 2013.

Hirsch, E. and Koren, I.: Record-breaking aerosol levels explained by smoke injection into the stratosphere, Science, 371, 1269–1274, https://doi.org/10.1126/science.abe1415, 2021.

Hodshire, A. L., Akherati, A., Alvarado, M. J., Brown-Steiner, B., Jathar, S. H., Jimenez, J. L., Kreidenweis, S. M., Lonsdale, C. R., Onasch, T. B., Ortega, A. M., and Pierce, J. R.: Aging effects on biomass burning aerosol mass and composition: a critical review of field and laboratory studies, Environ. Sci. Technol., 53, 10007–10022, https://doi.org/10.1021/acs.est.9b02588, 2019.

Hoose, C. and Möhler, O.: Heterogeneous ice nucleation on atmospheric aerosols: a review of results from laboratory experiments, Atmos. Chem. Phys., 12, 9817–9854, https://doi.org/10.5194/acp-12-9817-2012, 2012.

Hopkins, R. J., Desyaterik, Y., Tivanski, A. V., Zaveri, R. A., Berkowitz, C. M., Tyliszczak, T., Gilles, M. K., and Laskin, A.: Chemical speciation of sulfur in marine cloud droplets and particles: Analysis of individual particles from the marine boundary layer over the California current, J. Geophys. Res.: Atmos., 113, 1–15, https://doi.org/10.1029/2007JD008954, 2008.

Inoue, J., Tobo, Y., Taketani, F., and Sato, K.: Oceanic supply of ice-nucleating particles and its

effect on ice cloud formation: A case study in the Arctic Ocean during a cold-air outbreak in early winter, Geophys. Res. Lett., 48, https://doi.org/10.1029/2021GL094646, 2021.

IPCC: Climate Change 2013: The Physical Science Basis. Contribution of Working Group I to the Fifth Assessment Report of the Intergovernmental Panel on Climate Change, Cambridge University Press, Cambridge, United Kingdom and New York, NY, USA, 2013.

IPCC: Climate change 2021: the physical science basis, Cambridge University Press, 2021.

Jang, E., Park, K.-T., Yoon, Y. J., Kim, T.-W., Hong, S.-B., Becagli, S., Traversi, R., Kim, J., and Gim, Y.: New particle formation events observed at the King Sejong Station, Antarctic Peninsula – Part 2: Link with the oceanic biological activities, Atmos. Chem. Phys., 19, 7595–7608, https://doi.org/10.5194/acp-19-7595-2019, 2019.

Jang, J., Park, J., Park, J., Yoon, Y. J., Dall' Osto, M., Park, K.-T., Jang, E., Lee, J. Y., Cho, K. H., and Lee, B. Y.: Ocean-atmosphere interactions: Different organic components across Pacific and Southern Oceans, Sci. Total Environ., 878, 1–12, https://doi.org/10/gs3zkw, 2023.

Kanji, Z. A., DeMott, P. J., Möhler, O., and Abbatt, J. P. D.: Results from the University of Toronto continuous flow diffusion chamber at ICIS 2007: instrument intercomparison and ice onsets for different aerosol types, Atmos. Chem. Phys., 11, 31–41, https://doi.org/10.5194/acp-11-31-2011, 2011.

Kanji, Z. A., Ladino, L. A., Wex, H., Boose, Y., Burkert-Kohn, M., Cziczo, D. J., and Krämer, M.: Overview of ice nucleating particles, Meteorol. Monogr., 58, 1.1-1.33, https://doi.org/10.1175/AMSMONOGRAPHS-D-16-0006.1, 2017.

Khvorostyanov, V. I. and Curry, J. A.: The theory of ice nucleation by heterogeneous freezing of deliquescent mixed CCN. Part I: Critical radius, energy, and nucleation rate, J. Atmos. Sci., 61, 2676–2691, https://doi.org/10/b7nhwf, 2004.

Knopf, D. A. and Alpert, P. A.: A water activity based model of heterogeneous ice nucleation kinetics for freezing of water and aqueous solution droplets, Faraday Discuss., 165, 513–534, https://doi.org/10.1039/c3fd00035d, 2013.

Knopf, D. A., Alpert, P. A., Wang, B., and Aller, J. Y.: Stimulation of ice nucleation by marine diatoms, Nat. Geosci., 4, 88–90, https://doi.org/10.1038/ngeo1037, 2011.

Knopf, D. A., Alpert, P. A., Wang, B., O' Brien, R. E., Kelly, S. T., Laskin, A., Gilles, M. K., and Moffet, R. C.: Microspectroscopic imaging and characterization of individually identified ice nucleating particles from a case field study, J. Geophys. Res.: Atmos., 119, 10,365-10,381, https://doi.org/10.1002/2014JD021866, 2014.

Knopf, D. A., Alpert, P. A., and Wang, B.: The role of organic aerosol in atmospheric ice nucleation: a review, ACS Earth Space Chem., 2, 168–202, https://doi.org/10.1021/acsearthspacechem.7b00120, 2018.

Knopf, D. A., Charnawskas, J. C., Wang, P., Wong, B., Tomlin, J. M., Jankowski, K. A., Fraund, M., Veghte, D. P., China, S., Laskin, A., Moffet, R. C., Gilles, M. K., Aller, J. Y., Marcus, M. A., Raveh-Rubin, S., and Wang, J.: Micro-spectroscopic and freezing characterization of ice-nucleating particles collected in the marine boundary layer in the eastern North Atlantic, Atmos. Chem. Phys., 22, 5377–5398, https://doi.org/10.5194/acp-22-5377-2022, 2022.

Knopf, D. A., Wang, P., Wong, B., Tomlin, J. M., Veghte, D. P., Lata, N. N., China, S., Laskin, A., Moffet, R. C., Aller, J. Y., Marcus, M. A., and Wang, J.: Physicochemical characterization of free troposphere and marine boundary layer ice-nucleating particles collected by aircraft in the eastern North Atlantic, Atmos. Chem. Phys., 23, 8659–8681, https://doi.org/10.5194/acp-23-8659-2023, 2023.

Koehler, K. A., DeMott, P. J., Kreidenweis, S. M., Popovicheva, O. B., Petters, M. D., Carrico, C. M., Kireeva, E. D., Khokhlova, T. D., and Shonija, N. K.: Cloud condensation nuclei and ice nucleation activity of hydrophobic and hydrophilic soot particles, Phys. Chem. Chem. Phys., 11, 7906–7920, https://doi.org/10.1039/b905334b, 2009.

Koop, T. and Zobrist, B.: Parameterizations for ice nucleation in biological and atmospheric systems, Phys. Chem. Chem. Phys., 11, 10839, https://doi.org/10.1039/b914289d, 2009.

Koop, T., Luo, B., Tsias, A., and Peter, T.: Water activity as the determinant for homogeneous ice nucleation in aqueous solutions, Nature, 406, 611–614, https://doi.org/10.1038/35020537, 2000.

Kulkarni, G., Sanders, C., Zhang, K., Liu, X., and Zhao, C.: Ice nucleation of bare and sulfuric acid-coated mineral dust particles and implication for cloud properties: Ice formation on dust particles, J. Geophys. Res.: Atmos., 119, 9993–10011, https://doi.org/10.1002/2014JD021567, 2014.

Kunwar, B., Pokhrel, A., Niwai, T., and Kawamura, K.: Spatial and longitudinal distributions of total carbon, nitrogen and sulfur together with water-soluble major ions in marine aerosols collected from the Western Pacific and Southern Ocean, J. Geophys. Res.: Atmos., 128, 1–23, https://doi.org/10.1029/2022JD037874, 2023.

Laskin, A., Iedema, M. J., and Cowin, J. P.: Quantitative time-resolved monitoring of nitrate formation in sea salt particles using a CCSEM/EDX single particle analysis, Environ. Sci. Technol., 36, 4948–4955, https://doi.org/10.1021/es020551k, 2002.

Laskin, A., Cowin, J. P., and Iedema, M. J.: Analysis of individual environmental particles using modern methods of electron microscopy and X-ray microanalysis, J. Electron. Spectrosc. Relat. Phenom., 150, 260–274, https://doi.org/10.1016/j.elspec.2005.06.008, 2006.

Laskin, A., Moffet, R. C., Gilles, M. K., Fast, J. D., Zaveri, R. A., Wang, B., Nigge, P., and Shutthanandan, J.: Tropospheric chemistry of internally mixed sea salt and organic particles: Surprising reactivity of NaCl with weak organic acids, J. Geophys. Res.: Atmos., 117, 1–12, https://doi.org/10.1029/2012JD017743, 2012.

Lata, N. N., Zhang, B., Schum, S., Mazzoleni, L., Brimberry, R., Marcus, M. A., Cantrell, W. H., Fialho, P., Mazzoleni, C., and China, S.: Aerosol composition, mixing state, and phase state of free tropospheric particles and their role in ice cloud formation, ACS Earth Space Chem., 5, 3499–3510, https://doi.org/10.1021/acsearthspacechem.1c00315, 2021.

Liu, X. and Penner, J. E.: Ice nucleation parameterization for global models, Meteorologische Zeitschrift, 499–514, https://doi.org/10/b3b83s, 2005.

Liu, Y., Minofar, B., Desyaterik, Y., Dames, E., Zhu, Z., Cain, J. P., Hopkins, R. J., Gilles, M. K., Wang, H., Jungwirth, P., and Laskin, A.: Internal structure, hygroscopic and reactive properties of mixed sodium methanesulfonate-sodium chloride particles, Phys. Chem. Chem. Phys., 13, 11846–11857, https://doi.org/10.1039/c1cp20444k, 2011.

MacKay, D. J. C.: Information theory, inference, and learning algorithms, Cambridge University Press, Cambridge, 628 pp., 2003.

McCluskey, C. S., Ovadnevaite, J., Rinaldi, M., Atkinson, J., Belosi, F., Ceburnis, D., Marullo, S., Hill, T. C. J., Lohmann, U., Kanji, Z. A., O' Dowd, C., Kreidenweis, S. M., and DeMott, P. J.: Marine and terrestrial organic ice-nucleating particles in pristine marine to continentally influenced Northeast Atlantic air masses, J. Geophys. Res.: Atmos., 123, 6196–6212, https://doi.org/10/gpjrfh, 2018a.

McCluskey, C. S., Hill, T. C. J., Humphries, R. S., Rauker, A. M., Moreau, S., Strutton, P. G., Chambers, S. D., Williams, A. G., McRobert, I., Ward, J., Keywood, M. D., Harnwell, J., Ponsonby, W., Loh, Z. M., Krummel, P. B., Protat, A., Kreidenweis, S. M., and DeMott, P. J.: Observations of ice nucleating particles over Southern Ocean waters, Geophys. Res. Lett., 45, 11–989, https://doi.org/10.1029/2018GL079981, 2018b.

McCoy, I. L., Bretherton, C. S., Wood, R., Twohy, C. H., Gettelman, A., Bardeen, C. G., and Toohey, D. W.: Influences of recent particle formation on Southern Ocean aerosol variability and low cloud properties, Journal of Geophysical Research: Atmospheres, 126, e2020JD033529, https://doi.org/10.1029/2020JD033529, 2021.

Möhler, O., Büttner, S., Linke, C., Schnaiter, M., Saathoff, H., Stetzer, O., Wagner, R., Krämer, M., Mangold, A., Ebert, V., and Schurath, U.: Effect of sulfuric acid coating on heterogeneous ice nucleation by soot aerosol particles, J. Geophys. Res.: Atmos., 110, 1–12, https://doi.org/10.1029/2004JD005169, 2005a.

Möhler, O., Linke, C., Saathoff, H., Schnaiter, M., Wagner, R., Mangold, A., Krämer, M., and Schurath, U.: Ice nucleation on flame soot aerosol of different organic carbon content, Meteorol. Zeitschrift, 14, 477–484, https://doi.org/10.1127/0941-2948/2005/0055, 2005b.

Murray, B. J., O' Sullivan, D., Atkinson, J. D., and Webb, M. E.: Ice nucleation by particles immersed in supercooled cloud droplets, Chem. Soc. Rev., 41, 6519–6554, https://doi.org/10.1039/c2cs35200a, 2012.

Myriokefalitakis, S., Vignati, E., Tsigaridis, K., Papadimas, C., Sciare, J., Mihalopoulos, N.,

Facchini, M. C., Rinaldi, M., Dentener, F. J., Ceburnis, D., Hatzianastasiou, N., O' Dowd, C. D., van Weele, M., and Kanakidou, M.: Global modeling of the oceanic source of organic aerosols, Adv. Meteorol., 2010, 1–16, https://doi.org/10.1155/2010/939171, 2010.

Niemand, M., Möhler, O., Vogel, B., Vogel, H., Hoose, C., Connolly, P., Klein, H., Bingemer, H., DeMott, P., Skrotzki, J., and Leisner, T.: A particle-surface-area-based parameterization of immersion freezing on desert dust particles, J. Atmos. Sci., 69, 3077–3092, https://doi.org/10/f4bkkr, 2012.

O' Brien, R. E., Wang, B., Laskin, A., Riemer, N., West, M., Zhang, Q., Sun, Y., Yu, X., Alpert, P., Knopf, D. A., Gilles, M. K., and Moffet, R. C.: Chemical imaging of ambient aerosol particles: Observational constraints on mixing state parameterization, J. Geophys. Res.: Atmos., 120, 9591–9605, https://doi.org/10.1002/2015JD023480, 2015.

Palm, B. B., Peng, Q., Fredrickson, C. D., Lee, B. H., Garofalo, L. A., Pothier, M. A., Kreidenweis, S. M., Farmer, D. K., Pokhrel, R. P., Shen, Y., Murphy, S. M., Permar, W., Hu, L., Campos, T. L., Hall, S. R., Ullmann, K., Zhang, X., Flocke, F., Fischer, E. V., and Thornton, J. A.: Quantification of organic aerosol and brown carbon evolution in fresh wildfire plumes, Proc. Natl. Acad. Sci. U.S.A., 117, 29469–29477, https://doi.org/10.1073/pnas.2012218117, 2020.

Park, J., Dall' Osto, M., Park, K., Gim, Y., Kang, H. J., Jang, E., Park, K.-T., Park, M., Yum, S. S., Jung, J., Lee, B. Y., and Yoon, Y. J.: Shipborne observations reveal contrasting Arctic marine, Arctic terrestrial and Pacific marine aerosol properties, Atmos. Chem. Phys., 20, 5573–5590, https://doi.org/10.5194/acp-20-5573-2020, 2020.

Park, J. Y., Lim, S., and Park, K.: Mixing state of submicrometer sea spray particles enriched by insoluble species in bubble-bursting experiments, J. Atmos. Ocean. Technol., 31, 93–104, https://doi.org/10.1175/JTECH-D-13-00086.1, 2014.

Primm, K. M., Schill, G. P., Veghte, D. P., Freedman, M. A., and Tolbert, M. A.: Depositional ice nucleation on NX illite and mixtures of NX illite with organic acids, J. Atmos. Chem., 74, 55–69, https://doi.org/10.1007/s10874-016-9340-x, 2017.

Pruppacher, H. R. and Klett, J. D.: Microphysics of clouds and precipitation, Springer Netherlands, Dordrecht, 954 pp., https://doi.org/10.1007/978-0-306-48100-0, 2010.

Riemer, N. and West, M.: Quantifying aerosol mixing state with entropy and diversity measures, Atmos. Chem. Phys., 13, 11423–11439, https://doi.org/10.5194/acp-13-11423-2013, 2013.

Riemer, N., Ault, A. P., West, M., Craig, R. L., and Curtis, J. H.: Aerosol mixing state: measurements, modeling, and impacts, Rev. Geophys., 57, 187–249, https://doi.org/10.1029/2018RG000615, 2019.

Rolph, G., Stein, A., and Stunder, B.: Real-time environmental applications and display system: ready, Environ. Model Softw., 95, 210–228, https://doi.org/10.1016/j.envsoft.2017.06.025, 2017.

Schill, G. P. and Tolbert, M. A.: Heterogeneous ice nucleation on simulated sea-spray aerosol using Raman microscopy, J. Phys. Chem. C, 118, 29234–29241, https://doi.org/10.1021/jp505379j, 2014.

Song, Y., Qiao, F., Liu, J., Shu, Q., Bao, Y., Wei, M., and Song, Z.: Effects of sea spray on large-scale climatic features over the Southern Ocean, J. Clim., 35, 4645–4663, https://doi.org/10.1175/JCLI-D-21-0608.1, 2022.

Stein, A. F., Draxler, R. R., Rolph, G. D., Stunder, B. J. B., Cohen, M. D., and Ngan, F.: NOAA' s HYSPLIT atmospheric transport and dispersion modeling system, Bull. Am. Meteorol. Soc., 96, 2059–2077, https://doi.org/10.1175/BAMS-D-14-00110.1, 2015.

Su, B., Wang, T., Zhang, G., Liang, Y., Lv, C., Hu, Y., Li, L., Zhou, Z., Wang, X., and Bi, X.: A review of atmospheric aging of sea spray aerosols: Potential factors affecting chloride depletion, Atmos. Environ., 290, 1–24, https://doi.org/10.1016/j.atmosenv.2022.119365, 2022.

Tang, M., Cziczo, D. J., and Grassian, V. H.: Interactions of water with mineral dust aerosol: water adsorption, hygroscopicity, cloud condensation, and ice nucleation, Chem. Rev., 116, 4205–4259, https://doi.org/10.1021/acs.chemrev.5b00529, 2016.

Tang, M. J., Schuster, G., and Crowley, J. N.: Heterogeneous reaction of N_2O_5 with illite and Arizona test dust particles, Atmos. Chem. Phys., 14, 245–254, https://doi.org/10.5194/acp-14-245-2014, 2014.

Tomlin, J. M., Jankowski, K. A., Veghte, D. P., China, S., Wang, P., Fraund, M., Weis, J., Zheng, G., Wang, Y., Rivera-Adorno, F., Raveh-Rubin, S., Knopf, D. A., Wang, J., Gilles, M. K., Moffet, R. C., and Laskin, A.: Impact of dry intrusion events on the composition and mixing state of particles during the winter Aerosol and Cloud Experiment in the Eastern North Atlantic (ACE-ENA), Atmos. Chem. Phys., 21, 18123–18146, https://doi.org/10.5194/acp-21-18123-2021, 2021.

Tomlin, J. M., Weis, J., Veghte, D. P., China, S., Fraund, M., He, Q., Reicher, N., Li, C., Jankowski, K. A., Rivera-Adorno, F. A., Morales, A. C., Rudich, Y., Moffet, R. C., Gilles, M. K., and Laskin, A.: Chemical composition and morphological analysis of atmospheric particles from an intensive bonfire burning festival, Environ. Sci.: Atmos., 2, 616–633, https://doi.org/10.1039/D2EA00037G, 2022.

Vali, G.: Qauantitative evaluation of experimental results on the heterogeneous freezing nucleation of supercooled liquids, J. Atmos. Sci., 28, 402–409, https://doi.org/10.1175/1520-0469(1971)028<0402:QEOERA>2.0.CO;2, 1971.

Wagner, R., Kaufmann, J., Möhler, O., Saathoff, H., Schnaiter, M., Ullrich, R., and Leisner, T.: Heterogeneous ice nucleation ability of NaCl and sea salt aerosol particles at cirrus temperatures, J. Geophys. Res.: Atmos., 123, 2841–2860, https://doi.org/10.1002/2017JD027864, 2018.

Wang, B. and Knopf, D. A.: Heterogeneous ice nucleation on particles composed of humic-

like substances impacted by O_3, J. Geophys. Res.: Atmos., 116, 1–14, https://doi.org/10.1029/2010JD014964, 2011.

Wang, B., Laskin, A., Roedel, T., Gilles, M. K., Moffet, R. C., Tivanski, A. V., and Knopf, D. A.: Heterogeneous ice nucleation and water uptake by field-collected atmospheric particles below 273 K, J. Geophys. Res.: Atmos., 117, 1–15, https://doi.org/10.1029/2012JD017446, 2012a.

Wang, B., Lambe, A. T., Massoli, P., Onasch, T. B., Davidovits, P., Worsnop, D. R., and Knopf, D. A.: The deposition ice nucleation and immersion freezing potential of amorphous secondary organic aerosol: Pathways for ice and mixed-phase cloud formation, J. Geophys. Res.: Atmos., 117, 1–12, https://doi.org/10.1029/2012JD018063, 2012b.

Wang, B., O' Brien, R. E., Kelly, S. T., Shilling, J. E., Moffet, R. C., Gilles, M. K., and Laskin, A.: Reactivity of liquid and semisolid secondary organic carbon with chloride and nitrate in atmospheric aerosols, J. Phys. Chem. A, 119, 4498–4508, https://doi.org/10.1021/jp510336q, 2015.

Wang, B., Harder, T. H., Kelly, S. T., Piens, D. S., China, S., Kovarik, L., Keiluweit, M., Arey, B. W., Gilles, M. K., and Laskin, A.: Airborne soil organic particles generated by precipitation, Nat. Geosci., 9, 433–437, https://doi.org/10.1038/ngeo2705, 2016a.

Wang, B., Knopf, D. A., China, S., Arey, B. W., Harder, T. H., Gilles, M. K., and Laskin, A.: Direct observation of ice nucleation events on individual atmospheric particles, Phys. Chem. Chem. Phys., 18, 29721–29731, https://doi.org/10.1039/C6CP05253C, 2016b.

Welti, A., Lüönd, F., Stetzer, O., and Lohmann, U.: Influence of particle size on the ice nucleating ability of mineral dusts, Atmos. Chem. Phys., 9, 6705–6715, https://doi.org/10.5194/acp-9-6705-2009, 2009.

Welti, A., Bigg, E. K., DeMott, P. J., Gong, X., Hartmann, M., Harvey, M., Henning, S., Herenz, P., Hill, T. C. J., Hornblow, B., Leck, C., Löffler, M., McCluskey, C. S., Rauker, A. M., Schmale, J., Tatzelt, C., van Pinxteren, M., and Stratmann, F.: Ship-based measurements of ice nuclei concentrations over the Arctic, Atlantic, Pacific and Southern oceans, Atmos. Chem. Phys., 20, 15191–15206, https://doi.org/10.5194/acp-20-15191-2020, 2020.

Wilson, T. W., Ladino, L. A., Alpert, P. A., Breckels, M. N., Brooks, I. M., Browse, J., Burrows, S. M., Carslaw, K. S., Huffman, J. A., Judd, C., Kilthau, W. P., Mason, R. H., McFiggans, G., Miller, L. A., Nájera, J. J., Polishchuk, E., Rae, S., Schiller, C. L., Si, M., Temprado, J. V., Whale, T. F., Wong, J. P. S., Wurl, O., Yakobi-Hancock, J. D., Abbatt, J. P. D., Aller, J. Y., Bertram, A. K., Knopf, D. A., and Murray, B. J.: A marine biogenic source of atmospheric ice-nucleating particles, Nature, 525, 234–238, https://doi.org/10.1038/nature14986, 2015.

Xiao, H. S., Dong, J. L., Wang, L. Y., Zhao, L. J., Wang, F., and Zhang, Y. H.: Spatially resolved micro-Raman observation on the phase separation of effloresced sea salt droplets, Environ. Sci. Technol., 42, 8698–8702, https://doi.org/10.1021/es801181f, 2008.

Yakobi-Hancock, J. D., Ladino, L. A., and Abbatt, J. P. D.: Feldspar minerals as efficient deposition ice nuclei, Atmos. Chem. Phys., 13, 11175–11185, https://doi.org/10.5194/acp-13-11175-2013, 2013.

Yan, J., Jung, J., Zhang, M., Bianchi, F., Tham, Y. J., Xu, S., Lin, Q., Zhao, S., Li, L., and Chen, L.: Uptake selectivity of methanesulfonic acid (MSA) on fine particles over polynya regions of the Ross Sea, Antarctica, Atmos. Chem. Phys., 20, 3259–3271, https://doi.org/10.5194/acp-20-3259-2020, 2020.

Yao, Y., Curtis, J. H., Ching, J., Zheng, Z., and Riemer, N.: Quantifying the effects of mixing state on aerosol optical properties, Atmos. Chem. Phys., 22, 9265–9282, https://doi.org/10/gr2nbf, 2022.

Zhang, M., Chen, L., Xu, G., Lin, Q., and Liang, M.: Linking phytoplankton activity in polynyas and sulfur aerosols over Zhongshan Station, East Antarctica, J. Atmos. Sci., 72, 4629–4642, https://doi.org/10.1175/JAS-D-15-0094.1, 2015.